Signal Processing Systems
Mekelweg 4,
2628 CD Delft
The Netherlands
https://sps.ewi.tudelft.nl/

SPS-2023-5232481

M.Sc. Thesis

Comparative analysis of clutter filtering techniques on freehand μDoppler ultrasound imaging

Xuan Gao

Abstract

Micro-Doppler (μDoppler) ultrasound imaging is a high frame rate ultrasound imaging modality that provides high spatiotemporal resolution ultrasound images of blood flow. It is sensitive to slow blood flow and particularly suitable for capturing fast-changing phenomena like rapid blood flow. Clutter filtering is an essential step in μDoppler data processing to reject tissue clutter signals and keep blood flow information as much as possible. 3D freehand μDoppler imaging is an emerging ultrasound technique that can construct full spatial vasculature images with a panoramic view that conventional 2D ultrasound is not able to provide. As freehand implies the continuous and nonuniform movement of the probe, it becomes more challenging for clutter filtering to acquire high-quality images.

This thesis explores and compares different state-of-art clutter filtering techniques on freehand in-vivo μDoppler imaging of the human brain. Specifically, Singular Value Decomposition (SVD), Robust Principle Component Analysis (Robust PCA), and Independent Component Analysis (ICA) clutter filtering techniques have been investigated. The aim is to test and compare their performance on in-vivo μDoppler ultrasound data with freehand probe movement and understand how freehand motion affects the threshold selection criteria. Besides that, a newly proposed method that combines ICA clutter filtering and clustering is included in this thesis to bring another perspective for sorting independent components corresponding to blood flow and rejecting unwanted ones consisting mostly of tissue clutter signals.

Faculty of Electrical Engineering, Mathematics and Computer Science
Delft University of Technology

Comparative analysis of clutter filtering techniques on freehand μDoppler ultrasound imaging

---

THESIS

submitted in partial fulfillment of the
requirements for the degree of

MASTER OF SCIENCE

in

ELECTRICAL ENGINEERING

by

Xuan Gao
born in Jinan Shandong, China

This work was performed in:

Signal Processing Systems Group
Department of Microelectronics
Faculty of Electrical Engineering, Mathematics and Computer Science
Delft University of Technology

Delft University of Technology

Copyright © 2023 Signal Processing Systems Group
All rights reserved.

Delft University of Technology
Department of
Microelectronics

The undersigned hereby certify that they have read and recommend to the Faculty of Electrical Engineering, Mathematics and Computer Science for acceptance a thesis entitled **“Comparative analysis of clutter filtering techniques on freehand μDoppler ultrasound imaging”** by **Xuan Gao** in partial fulfillment of the requirements for the degree of **Master of Science**.

Dated: 04-07-2023

Chairman:

dr. B. Hunyadi

Advisors:

dr. B. Hunyadi

Luuk Verhoef

Committee Members:

dr. T. Costa

Acknowledgments

In November 2022, I began working on my thesis at CUBE, Erasmus MC. I would like to first thank Prof. Alle-Jan van der Veen and Dr. Pieter Kruizinga for introducing me to this group. During my thesis work at CUBE, my daily supervisor Luuk Verhoef has guided me all the way with patience and support which I feel deeply grateful and thankful for. My thesis journey would not have been possible without his help and support. The eight months I spent working on my thesis at CUBE have been the happiest time of my Master's study, and this experience will remain unforgettable. I not only gained knowledge in ultrasound, but also drew inspiration from the people around me, and enjoyed the happiness of talking to them during lunch break. Their passion and dedication to their work have motivated me to pursue my own passions and interests in the future. All these joyful moments will be etched in my memory.

I would like to express my heartful gratitude to my TU Delft supervisor Dr. Bori Hunyadi for her assistance in my thesis writing. She has provided me with thorough suggestions and guidance during our bi-weekly meetings. Our meetings were fruitful and steered me in the right direction. I would also like to thank my family for their unconditional love and support. Besides that, I would like to thank my friends who accompanied me along this journey for the past two years.

Xuan Gao
Delft, The Netherlands
04-07-2023

Contents

List of Figures

List of Tables

Introduction

1

Medical ultrasound using conventional ultrasonography emerged in the 1970s [8]. More than thirty years ago, the concept of ultrafast ultrasound imaging was introduced [9]. Ultrafast ultrasound imaging, also known as micro-Doppler (μDoppler) ultrasound imaging, is a high frame rate (HFR) ultrasound imaging technique that involves Doppler processing of microvascular hemodynamics, providing high spatiotemporal resolution images [10, 11]. The underlying principle is to study the temporal variations of signals backscattered by blood motions using repeated ultrasonic pulses [12]. It is a rapidly developing non-invasive method used for imaging vasculature in neuroscience research.

Compared to conventional color flow imaging, μDoppler imaging has a much higher sensitivity due to the combined sensitivity gains resulting from coherent planewave compounding [13]. Its high sensitivity is suitable for slow blood flow and its ability to achieve extremely high frame rates using planewave transmission makes it particularly suitable for capturing fast-changing phenomena like rapid blood flow. It also offers high spatiotemporal resolution and high signal-to-noise ratio (SNR), contributing to enhanced image quality. These advantages bring value to many clinical techniques and applications such as functional ultrasound (fUS), vascular anatomy, brain vascular imaging, tumor resection, and surgical decision-making.

μDoppler data processing involves planewave transmission, raw radio frequency (RF) data acquisition, image reconstruction, clutter filtering, and power estimation. Raw RF data is acquired using planewave transmission, then the reconstructed image is filtered using clutter filtering techniques. After that, the power intensity of the Doppler signal at each pixel over the temporal dimension is summed over to reconstruct a power Doppler image. Without clutter filtering, the reconstructed image cannot be directly used for image visualization as it contains a significant amount of tissue clutter and noise. The beamformed raw data is represented by complex variables consisting of blood flow signals, clutter signals, and electronic/thermal noise [14]. Blood signals contain useful information for brain activity and vasculature analysis, while clutter and noisy signals mainly consist of tissue motion and noise disturbances, which need to be removed.

2D ultrasound imaging with visualization of the region of interest has been widely used [15, 16]. However, 2D ultrasound imaging alone cannot provide orientation or anatomical information, thus limiting its diagnostic accuracy. To overcome this limitation, 3D ultrasound imaging aims to construct full spatial anatomical images, providing physicians with a panoramic view. 3D freehand ultrasound imaging involves obtaining 3D ultrasound images while continuously moving the probe [4] by hand. As the probe moves, image filtering becomes more complex and challenging, requiring adaptive clutter filtering techniques to acquire high-quality images.

Therefore, clutter filtering is crucial to remove tissue motion and noise disturbances, especially for freehand μDoppler imaging with probe movement. Conventional clutter filters can be applied to the beamformed data by simply using high-pass and low-pass filters on the power spectrum. Tissue signals have high amplitude but low frequency, blood signals have higher frequency but low amplitude, and thermal noise has low amplitude and high frequency. However, these methods are not highly effective, especially when distinguishing between slow-velocity small blood vessels and tissue motion due to overlapped subspaces. Singular value decomposition (SVD) makes use of different spatiotemporal features of tissue and blood signals and significantly outperforms conventional clutter filters based on high-pass temporal filtering [14]. Other clutter filtering techniques include Robust PCA clutter filtering, which decomposes the signal matrix into a sum of a low-rank matrix and a sparse matrix [17], ICA clutter filtering, which seeks to transform the data onto a basis with statistically independent vectors [18, 19], Project Approximation Subspace Tracking (PAST) [20], and Nonnegative Matrix Factorization [21]. After clutter filtering, the mean intensity of the Doppler signal at each pixel is extracted to generate a power Doppler image for analysis.

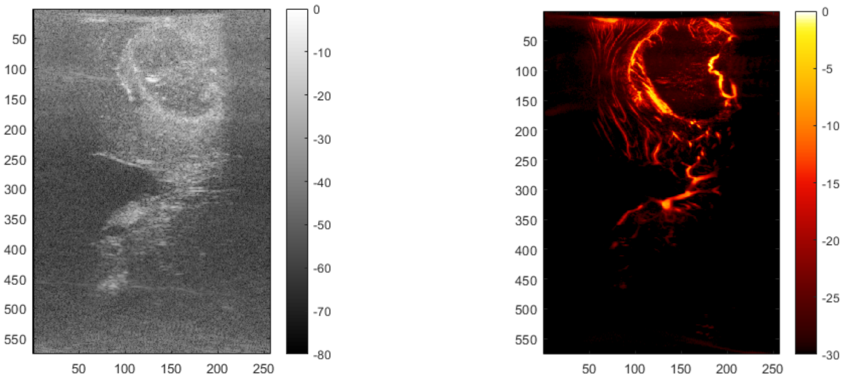

(a) B-mode image

(b) Power Doppler image

Figure 1.1: An example of the comparison between a B-mode image without clutter filtering and a power Doppler image using clutter filtering. After planewave transmission and raw RF data acquisition, a B-mode image is reconstructed as figure (a). After clutter filtering and power estimation, a power Doppler image is reconstructed as figure (b).

1.1 Research question

The objective of this thesis is to explore and compare different state-of-art clutter filtering techniques on freehand μDoppler imaging.

The following questions are investigated:

1. How to optimally estimate the boundary between the tissue subspace and blood flow subspace using spatiotemporal SVD clutter filtering for μDoppler imaging?

As tissue and blood flow subspaces are not always easy to separate, we hypothesize that the difficulty of finding an optimal threshold comes from the fact that there is an arbitrary orthogonality constraint for SVD clutter filtering. Later on, Robust PCA and ICA clutter filtering techniques were explored in comparison with SVD clutter filtering. More sub-questions involve:

2. How to illustrate that tissue and blood flow have overlapped subspaces on the eigen-domain?
3. How does freehand motion affect the threshold selection criteria?
4. How is the performance of Robust PCA and ICA clutter filtering compared to SVD clutter filtering for μDoppler imaging?
5. How to make fair comparisons and evaluate image quality among different clutter filtering techniques?

1.2 Outline

Chapter 2 gives background knowledge of Doppler imaging, μDoppler data processing, and 3D freehand ultrasound imaging. μDoppler data processing involves planewave transmission, raw data acquisition, image reconstruction, clutter filtering, and power estimation.

Chapter 3 delivers the methodology of state-of-art clutter filtering techniques: SVD, Robust PCA, and ICA clutter filtering. In SVD clutter filtering, tissue and noise can be rejected by discarding the largest singular components which mainly contain tissue, and discarding the smallest singular components which mainly contain noise. There are several methods of finding the rejection threshold: arbitrary thresholding, singular value estimators, spatial singular vector estimators, and temporal singular vector estimators. Robust PCA clutter filtering decomposes the mixed signal matrix into one low-rank matrix and one sparse matrix. It assumes that the tissue matrix has a low-rank structure and blood flow matrix is more sparse. ICA clutter filtering seeks to transform the data onto a basis with statistically independent vectors. Independent sources corresponding to blood flow can be clustered by the hierarchical agglomerative clustering method and then the power is estimated along temporal dimension to reconstruct a power Doppler image.

Chapter 4 illustrates and analyses the results from three clutter filtering techniques explained in Chapter 3. For SVD clutter filtering, the results consist of the effect of probe movement on threshold choices, overlapped subspaces on eigen-domain, trade-off choices between ensemble sizes, threshold selections, and image quality. The results of Robust PCA clutter filtering include the choices of λ and μ on threshold selection. ICA clutter filtering results contain the independent component classification and comparisons with SVD clutter filtering.

Chapter 5 discusses research questions that include challenges and uncertainties on how to decide thresholds to distinguish tissue and blood flow, how to decide ensemble lengths for different clutter filtering techniques, how to tune parameters for Robust PCA clutter filtering, how to decide the number of independent components, how to sort independent sources corresponding to blood flow signals, how to make fair comparisons for the images filtered by different techniques, and also give future work suggestions.

Chapter 6 gives conclusions on the thesis work.

Background

2

2.1 Doppler imaging

2.1.1 Doppler effect

There are A-mode (amplitude-mode), B-mode (brightness-mode), M-mode (motion-mode), and Doppler-mode in ultrasound imaging systems. Doppler-mode imaging is used to estimate blood flow by detecting the wave frequency change bounced back from blood vessels. The transducer works both as a transmitter and a receiver. A higher-frequency sound wave is reflected back when the red blood cell approaches the probe. When cells move away from the probe, a lower-Doppler frequency wave is reflected. Fig. 2.1 shows the Doppler effect diagram. Red blood cell movement gives rise to the Doppler effect.

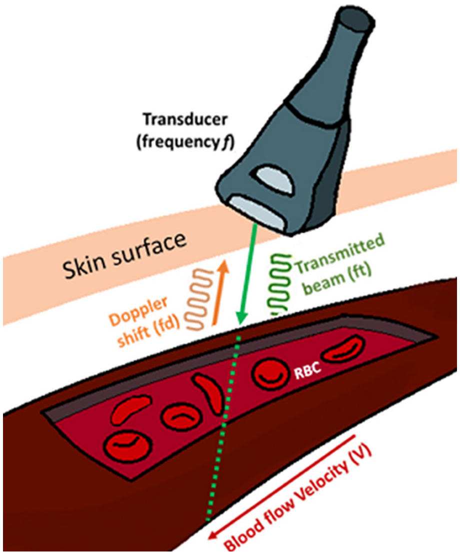

Figure 2.1: Diagram of Doppler effect [1]. Each red blood cell gives rise to a Doppler shift. The transducer transmits Doppler signals and receives the back-scattered signals from red blood cells (RBCs).

The Doppler shift equation 2.1 is shown as [22]:

$$F_d = F_r - F_t = \frac{2 \cdot F_t \cdot V \cdot \cos\theta}{c} \tag{2.1}$$

Here, F_d is the Doppler frequency shift signal. F_r is the received/reflected frequency. F_t is the transducer/transmission frequency. V is the velocity of blood cells. θ is the angle between the transducer and the blood cell. c is the sound speed in the tissue medium. As the waves travel from the transducer and then get reflected back, there is a factor two here for the round trip. Doppler shift is measured in Hertz (Hz).

When blood cells V move faster, the Doppler shift is larger. The strength of the Doppler shift also depends on the amount of moving cells. The angle θ between the transducer and RBCs has an effect on the Doppler shift. The Doppler shift wave reaches the largest when the angle is the smallest (zero degrees). In clinical practice, however, the probe is usually placed at around 60 degrees due to some considerations [1].

2.1.2 Color Doppler imaging

Color Doppler imaging is a classic Doppler sonogram. The encoding method of most color Doppler scanners is the estimation of the mean Doppler frequency shift at a specific position and representing it in color [23]. In color Doppler imaging, the speed and direction of the blood flow are displayed. The red color represents a positive shift (blood cells moving toward the probe), while the blue color represents a negative shift (blood cells moving away from the probe). Color Doppler imaging has had a big influence on ultrasonography. However, there are also some limitations. The biggest weakness of this conventional Doppler ultrasound is the lack of sensitivity [24,25], which is hard to detect small blood vessels (an example is shown in Figure 2.2).

2.1.3 Power Doppler imaging

Power Doppler imaging, also known as amplitude-mode color Doppler imaging or color Doppler energy [25], was developed after color Doppler imaging to detect small blood vessels and flow with low velocity. It has three times more sensitivity than conventional color Doppler imaging. Instead of encoding the mean Doppler frequency, power Doppler encodes the power in the Doppler technique and represents it in color. The mean power is calculated as equation 2.2 [24]:

$$PW(n_x, n_z) = \int |B(n_x, n_z, n_t)|^2 \, dt \tag{2.2}$$

Here, $PW(n_x, n_z)$ is the mean intensity power. $B\left(n_x, n_z, n_{t_i}\right)$ is the clutter filtered signal for each pixel (n_x, n_z) along time t_i. n_x, n_z, and n_{t_i} represent lateral, axial, and time coordinates respectively. N is the size of the ensemble. To increase the estimation of PW, the ensemble size must be large enough and the clutter in B must be reduced.

This technique weakens the noise disturbance in the imaging because the noise always has uniformly low power due to the standard SNR requirements of a Doppler scanner [23]. In this way, low power is represented only by a uniformly colored imaging background instead of a random distribution of colors which can lead to confusion in distinguishing any possible flows from noise. Compared with the mean frequency color Doppler, power Doppler is angle independent. As the total power is related to the number of moving scatters, it does not change with the angle of insonification. For color Doppler imaging, the mean Doppler shift will be larger at a small angle and will be smaller at a large angle, therefore, the probe angle should be carefully controlled for color Doppler to get a good image.

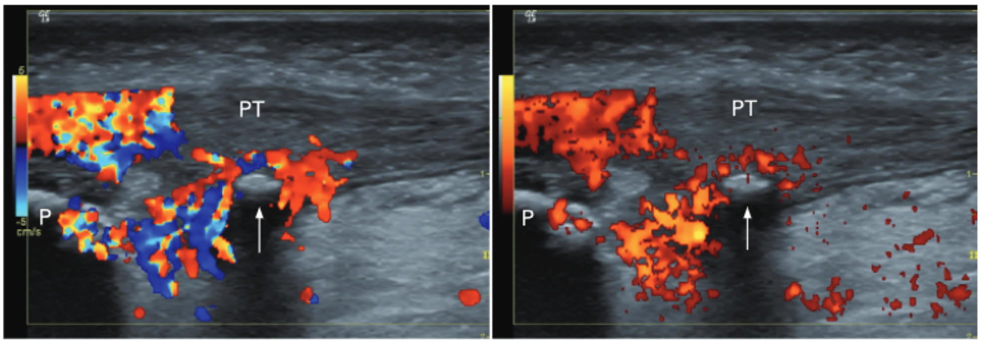

Figure 2.2: Color Doppler imaging (left) and Power Doppler imaging (right) comparison [2]. They show longitudinal scans of the patella tendon (PT) with Doppler activity in a patient with jumper's knee. Power Doppler imaging is more sensitive to blood vessels.

2.2 μDoppler data processing

There are five main steps in μDoppler data processing: planewave transmission, raw RF data acquisition, image reconstruction, clutter filtering, and power estimation. The steps and their functions are illustrated in Table 2.1.

In summary, planewave transmission utilizes unfocused beamforming instead of line-per-line focused beamforming. The transducer serves as both the transmitter and receiver. By detecting frequency changes induced by blood red cells, high-frame-rate beamformed raw RF data is acquired. To construct an image, a specific ensemble data size is initially selected. The Brightness-mode (B-mode) image is generated by summing the beamformed raw data over the temporal dimension. After image reconstruction, clutter filtering techniques are applied to enhance the image quality by reducing tissue clutters and other noise, while preserving the blood flow information. After summing the power of every pixel over the temporal dimension of the clutter filtered data, a power Doppler image (PDI) is reconstructed.

2.2.1 Planewave transmission

There are several beamforming options available in ultrasound imaging, including linear and phased array beamforming, multi-line transmission beamforming, plane and diverging wave beamforming, and synthetic aperture beamforming [26]. Conventional ultrasound imaging commonly utilizes line-per-line pulsed focused beamforming (Fig. 2.3A). The main drawback of this approach is its low frame rate.

To achieve the maximum frame rate, the number of transmission events required to form an image needs to be minimized. Planewave beamforming (Fig. 2.3B) can generate

μDoppler Processing Steps		
Steps	Processing	Function
1	Planewave transmission	Transmit and receive waves
2	Raw RF data acquisition	Acquire raw RF data
3	Image reconstruction	B-mode image reconstruction by summing over temporal dimension
4	Clutter filtering	Clutter filtering techniques (SVD, Robust PCA, ICA, etc.)
5	Power estimation	Power Doppler image reconstruction by estimating power for each pixel over temporal dimension

Table 2.1: μDoppler data processing

an image with a single transmission event, resulting in ultrafast ultrasound imaging with frame rates reaching thousands of hertz. However, this significant increase in frame rate comes at the expense of image quality. This issue is addressed by image compounding, where steering is applied before compounding. Steering refers to varying the transmission angles. By averaging frames with different steering angles, the final image is formed. While this reduces the frame rate by a factor equal to the number of angles, it improves spatial resolution, penetration depth, and signal-to-noise ratio (SNR) [26]. The number of angles can be adjusted for specific plane wave imaging applications. The extremely high frame rates achievable with plane wave imaging are well-suited for capturing fast-changing phenomena such as rapid blood flow. The beamformed data is then summed over temporal dimension to construct a B-mode image.

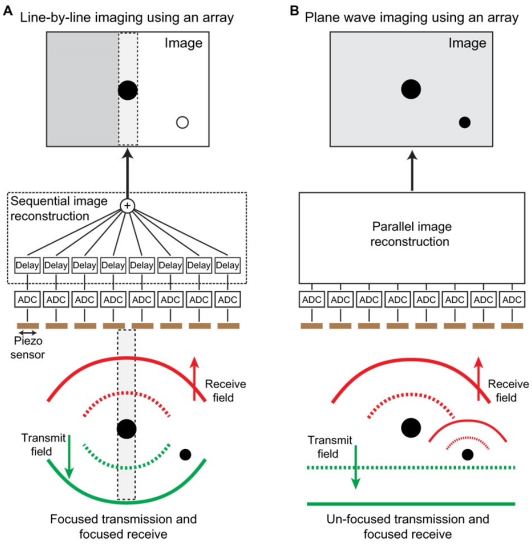

Figure 2.3: Comparison of line-per-line focused beam transmission (A) and planewave beam transmission (B) [3].

2.2.2 Doppler processing

Doppler processing involves clutter filtering and power estimation. Clutter filtering techniques aim to suppress clutter sources and noise while retaining blood flow information as much as possible. In some literature, clutter filtering techniques are also referred to as blind source separation techniques [18, 21] or clutter suppression techniques [27].

There are many clutter filtering techniques. Conventional high-pass filters make the assumption that moving tissue is concentrated in the low-frequency band and has a narrower bandwidth, while blood flow exhibits a broader bandwidth. However, this assumption is not effective for small blood vessels due to the overlap of the frequency spectrum. SVD-based clutter filtering relies on the assumption that tissue clutter, blood flow, and noise are uncorrelated and their subspaces are orthogonal. Tissue and noise are discriminated by discarding the largest singular components, which mainly contain tissue motion, and the smallest singular components, which mainly contain noise. SVD clutter filtering provides more robust and accurate clutter filtering in the presence of blood vessels. There are also other clutter filtering techniques such as Robust PCA or ICA clutter filtering. After summing the power of every pixel over the temporal dimension of the clutter filtered data, a power Doppler image is reconstructed. Chapter 3 will provide explanations of all the clutter filtering techniques used in this thesis.

2.3 3D freehand ultrasound imaging

Real-time 2D ultrasound imaging with visualization of the region of interest has been widely used [15, 16]. However, 2D ultrasound imaging alone cannot provide orientation or anatomical information, thus limiting its diagnostic accuracy. To overcome this limitation, 3D ultrasound imaging aims to construct full spatial anatomical images, providing physicians with a panoramic view. This technology not only facilitates accurate surgical instrument placement but also enhances image evaluation efficiency. 3D freehand ultrasound imaging involves obtaining 3D ultrasound images while continuously moving the probe [4]. As the probe moves, image filtering becomes more complex, requiring adaptive filtering techniques to acquire high-quality images.

The process of conducting 3D ultrasound imaging typically involves three main steps [28]: acquisition, reconstruction, and visualization. Filtered B-scans with their relative positions are acquired to reconstruct a volumetric grid, which can then be visualized using specific rendering techniques. A state-of-the-art real-time approach for 3D ultrasound imaging is to remap 2D frames to a 3D volume, combined with an optical tracking system [4, 28, 29]. An example of a 3D reconstructed vasculature is shown in Figure 2.5. Although the focus of this thesis is on 2D imaging, the inclusion of this 3D information provides users with a broader perspective on the application.

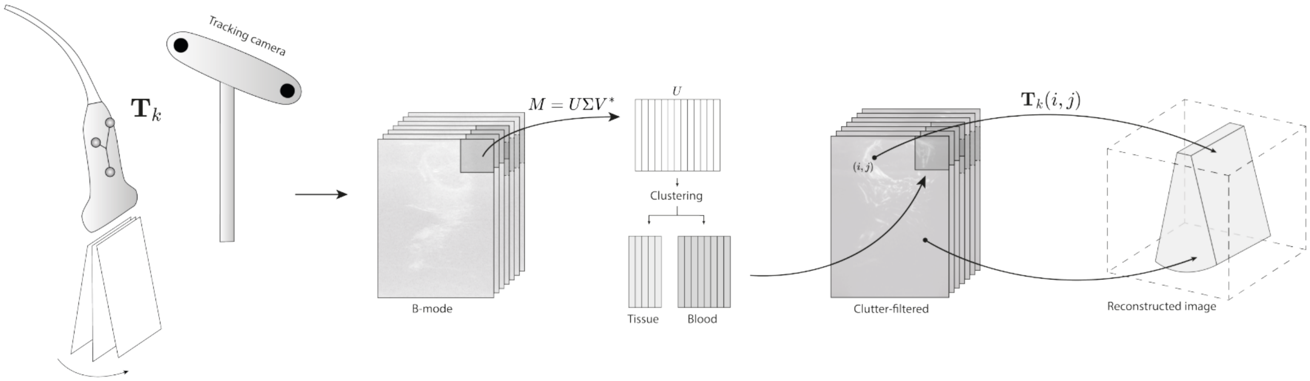

Figure 2.4: 3D Doppler imaging reconstruction using optical tracking [4]. Ultrasound data and optical tracking data are gathered by freehand scanning. After clutter filtering, the pixels of ultrasound data are mapped into a 3D space using the optical tracking data to reconstruct a 3D image.

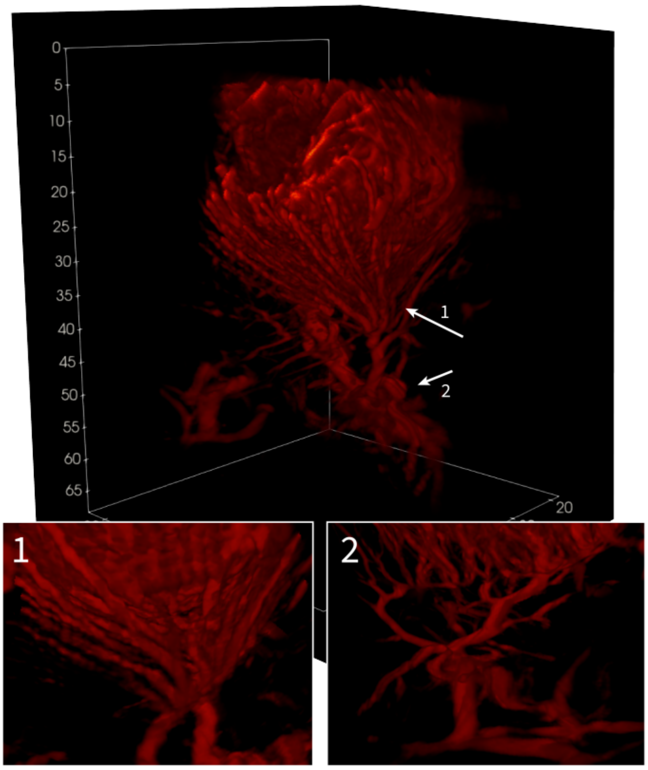

Figure 2.5: An example of from freehand Doppler imaging [4].

Clutter filtering techniques for μDoppler ultrasound imaging

3

As discussed in Chapter 2, ultrasound images are often affected by tissue clutter, electronic thermal noise, probe or patient motion, and other artifacts that can obscure blood vessel observations [21,30]. Consequently, ultrasound data can be represented as the superposition of:

$$X(n_x, n_z, n_t) = B(n_x, n_z, n_t) + C(n_x, n_z, n_t) + N(n_x, n_z, n_t) \tag{3.1}$$

where B, C, and N represent blood signals, clutter signals, and noise signals respectively, and n_x, n_z, and n_t represent lateral, axial, and time coordinates respectively. Clutter filtering techniques aim to suppress clutter sources and noise while retaining blood flow information as much as possible.

Chapter 3 covers the principles and algorithms of four clutter filtering techniques, including the most basic conventional frequency-based clutter filtering, widely used SVD based clutter filtering, low-rank-and-sparsity-assumed PCA based clutter filtering, and non-Gaussian ICA based clutter filtering. The techniques are compared among each other, and the results are further discussed in Chapters 4 and 5.

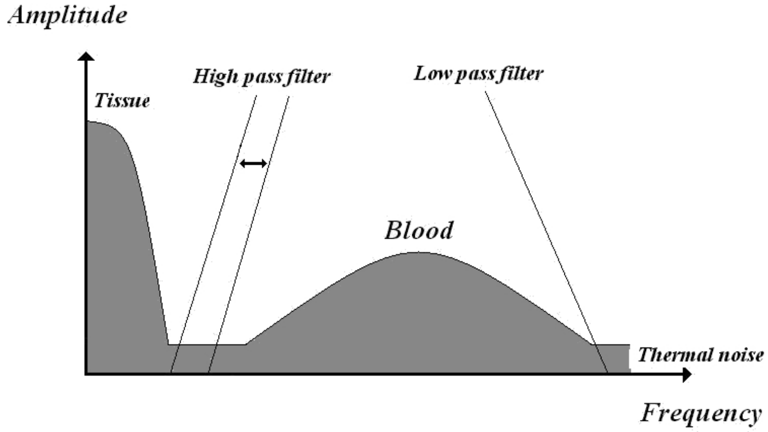

Figure 3.1: Frequency-based clutter filtering method using a high-pass filter to remove high-coherent tissue motion and a low-pass filter to discard low-coherent noise. [5]

3.1 Frequency-based clutter filtering technique

A frequency-based clutter filter (Figure 3.1) distinguishes tissue motion and blood vessels by considering their temporal properties. The ultrasound data is transformed into the frequency domain via discrete Fourier transform, and the frequency-based clutter filter aims to discard undesired signals within a certain frequency range. Tissue tends to move together and much slower than blood vessels. Therefore, tissue motion has a lower frequency and narrower frequency bandwidth, while blood flow has a higher frequency and broader frequency bandwidth. As a result, tissue, blood flow, and noise can be distinguished by using a high-pass filter that filters out tissue with a lower frequency characteristic and a low-pass filter that discards other noise with a higher frequency feature. However, tissue and blood flow separation is often not ideal for frequency-based clutter filters, especially for slow-flow blood vessels and fast tissue motions that overlap on the frequency domain.

3.2 SVD-based clutter filtering technique

SVD-based clutter filtering is used to remove tissue clutter and noise from ultrasound data. It relies on the assumption that tissue clutter, blood flow, and noise are uncorrelated and their subspaces are orthogonal. They are discriminated by discarding the largest singular components, which mainly contain tissue motion, and the smallest singular components, which mainly contain noise. This is because tissue tends to move together over time and therefore exhibits high spatial-temporal coherence. Noise signals are randomly distributed and thus have the lowest spatial-temporal coherence. Unlike frequency-based clutter filtering, SVD-based clutter filtering considers both spatial and temporal statistical properties by using the information in spatial singular vectors U, singular values Σ, and temporal singular vectors V.

The steps of SVD clutter filtering are illustrated in Figure 3.2. Firstly, a stack of beamformed frames with a size of (n_z, n_x, n_t) is selected and then reshaped into a Casorati matrix with a size of $(n_z \times n_x, n_t)$. The singular value decomposition is then applied to obtain a spatial singular vector matrix ($\mathbf{U}$) of size $(n_z \times n_x, n_t)$, a singular value matrix ($\mathbf{\Sigma}$) of size (n_t, n_t), and a temporal singular vector matrix ($\mathbf{V}$) of size (n_t, n_t) as:

$$X = U\Sigma V^{\mathrm{H}} \tag{3.2}$$

U and V are also eigenvectors of the covariance matrices XX^{H} and $X^{\mathrm{H}}X$:

$$\begin{aligned} XX^{\mathrm{H}} &= U\Sigma^2 U^{\mathrm{H}} \\ X^{\mathrm{H}}X &= V\Sigma^2 V^{\mathrm{H}} \end{aligned} \tag{3.3}$$

Tissue clutter suppression can be achieved by setting singular values with the highest magnitude and lowest magnitude to zero. The filtered dataset is reconstructed as:

$$X_{\text{filtered}} = \sum_{i=m}^{n} U_i \Sigma_{i,i} V_i^{\mathrm{H}}, \tag{3.4}$$

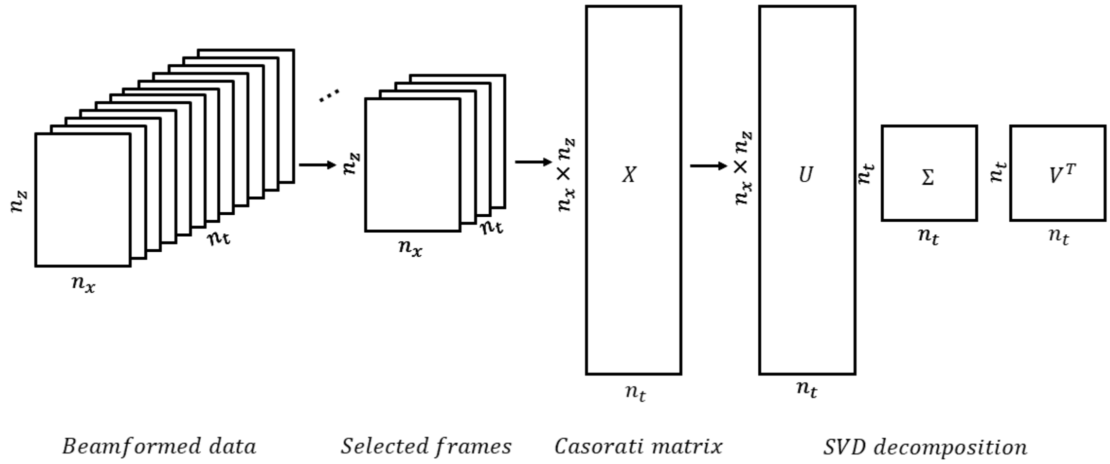

(a) A stack of beamformed frames with a size of (n_z, n_x, n_t) is selected and then reshaped into a Casorati matrix with a size of $(n_z \times n_x, n_t)$. SVD is then applied to obtain a spatial singular vector matrix ($\mathbf{U}$) of size $(n_z \times n_x, n_t)$, a singular value matrix ($\mathbf{\Sigma}$) of size (n_t, n_t), and a temporal singular vector matrix.

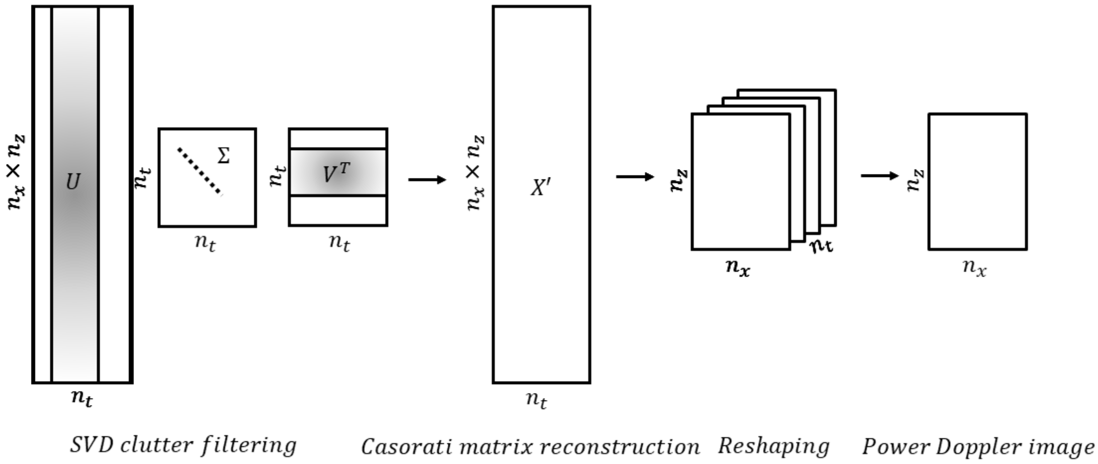

(b) After finding the appropriate thresholds for discarding unwanted signals, a matrix with a size of $(n_z \times n_x, n_t)$ is reconstructed using SVD. The resulting matrix is then reshaped into frames with a size of (n_z, n_x, n_t). The power of each pixel is calculated, and the values are summed over the time dimension to construct a power Doppler image.

Figure 3.2: SVD-based clutter filtering processing.

where m, n are cut-off thresholds. Singular values bigger than the m^{th} and smaller than the n^{th} values will be discarded.

After reshaping the Casorati matrix back to a stack of frames, the power of pixels is summed over time to construct a power Doppler image (Figure 3.2):

$$PW(n_x, n_z) = \int |B(n_x, n_z, n_t)|^2 \, dt \tag{3.5}$$

The thresholds vary with the different numbers of frames selected, the size of the selected filter region, and the starting point of the frames. If the threshold is set too large, some essential blood flow information may be not visible. If the threshold is too small, some unwanted tissue clutter may appear. To determine the appropriate thresholds for clutter filtering, various methods are used within SVD technique, including arbitrary thresholding, singular value estimation, spatial singular vector estimation, and temporal singular vector estimation.

3.2.1 Arbitrary thresholding

Arbitrary thresholding is based on intuition to decide how many percentages of singular components are to be discarded and retained. Different thresholds are tried and adjusted manually until the power Doppler image looks the most optimal. This method can provide a direct understanding of how different thresholds can affect image quality. However, when considering clutter filtering on many ensembles, it is time-consuming, lacks robustness, and does not consider blood flow and tissue characteristics in ultrasound signals.

3.2.2 Singular value (Σ) estimators

Singular value estimators are based on singular values. Each singular value gives a weighting to the contribution of each singular component in the whole dataset. The amplitude of singular values corresponding to tissue is much higher than the amplitude regarding blood flow. Baranger *et al.* [30] proposed three ways to decide the threshold based on singular values. The first way is by discarding the singular values above or below a certain magnitude (in dB). The second way is to calculate the ratio between the cumulative sum of singular values in the middle regime to the sum of the whole set. The threshold is set when the ratio reaches a certain level. The third way is to set the maximum acceleration point (when the second derivative of the signal equals zero) as the threshold.

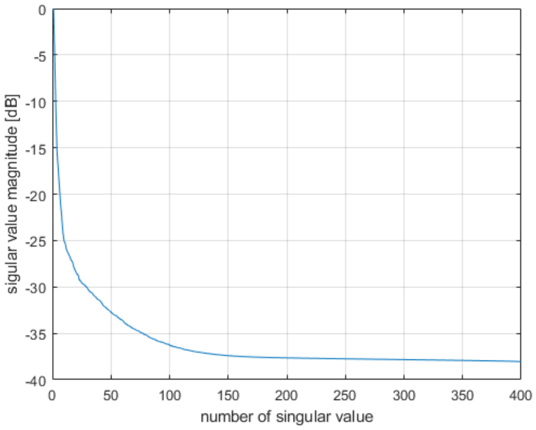

Figure 3.3: singular value energy plots in dB for the stationary dataset with the ensemble size 400. The curve is in a decreasing order based on the weighting of each singular value.

3.2.3 Spatial singular vector (U) estimators

Spatial singular vector estimators take into account the spatial characteristics of the ultrasound data. As tissue and blood flow have different spatial distributions, it is expected that their corresponding column vectors of **U** are correlated only within their subspaces. The noise is assumed to be white Gaussian and randomly spread, which results in uncorrelated spatial vectors for the noise [30].

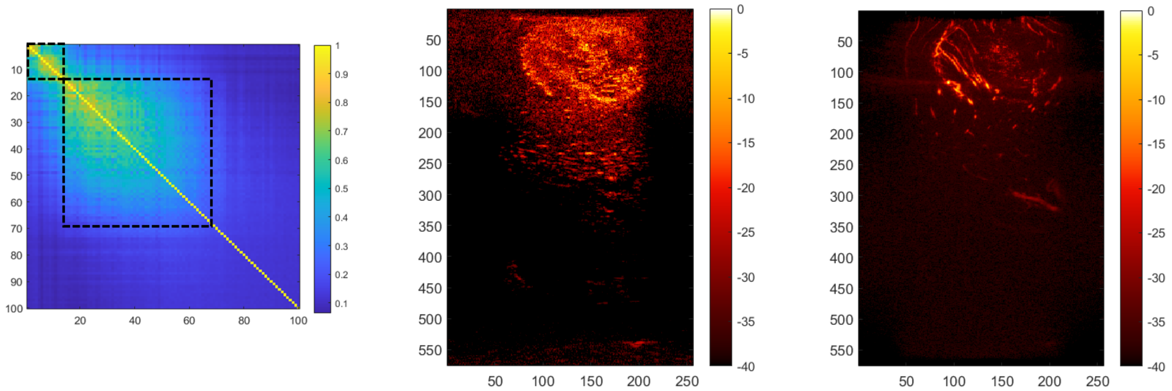

(a) Spatial similarity matrix of U. It represents the correlation among columns of the spatial singular vector

(b) The image reconstructed by the first 15 singular components

(c) The image reconstructed by the 16th to 65th singular components

Figure 3.4: Different subspaces due to different spatial distributions....

The correlation coefficient matrix **C** (also called spatial similarity matrix) of **U** is calculated as shown in Equation 3.6 [30], where n and m are the indices of each column of **U**, ranging from 1 to the ensemble size. p represents the elements within the same column vector. The absolute mean differences of each column are divided by the standard deviation and then normalized by dividing by the total number of column elements.

$$C(n,m) = \frac{1}{n_x \cdot n_z} \cdot \sum_{p}^{n_x \cdot n_z} \frac{\left(|u_n(p)| - \overline{|u_n|}\right) \cdot \left(|u_m(p)| - \overline{|u_m|}\right)}{\sigma_n \cdot \sigma_m} \tag{3.6}$$

The threshold selection is based on finding subspaces in the shape of squares in the similarity matrix of **U** (Figure 3.4a). This relies on the hypothesis that tissue and blood flow have different spatial distributions. Tissue and blood flow subspaces fall into two juxtaposed symmetrical square areas. These square areas can be separated by optimally fitting two squares to the spatial similarity matrix [30].

Besides finding square subspaces on the spatial similarity matrix of **U**, clustering algorithms such as K-means or hierarchical agglomerative clustering with connectivity constraint algorithms can be applied to column vectors of **U** to create clusters with similar spatial characteristics [4, 31].

3.2.4 Temporal singular vector (V) estimators

Temporal singular vector estimators determine the separation threshold between tissue and blood flow by looking at their temporal differences. Conventional high-pass filter distinguishes tissue and blood flow by considering their frequency ranges. Their same temporal characteristics can also be discovered in temporal singular vectors. Figure 3.5 shows the temporal variation for each singular component. Each column is one singular component varying over time. The variance of the first several columns is lower and is higher for the rest columns as their neighbor values tend to change faster.

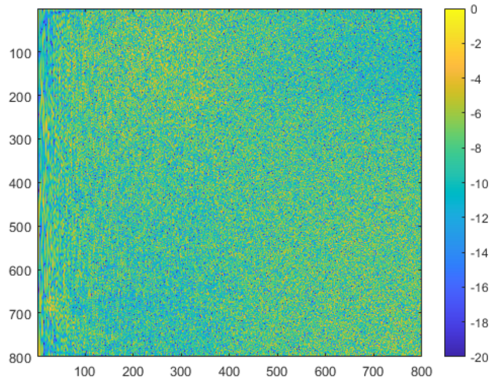

Figure 3.5: Temporal singular vector visualization

The variance corresponds to the frequency. Having higher variances also means that the value changes fast thus having higher frequencies. To find out their frequency range, the Fourier transform is applied to **V** to get the power spectrum density (PSD).

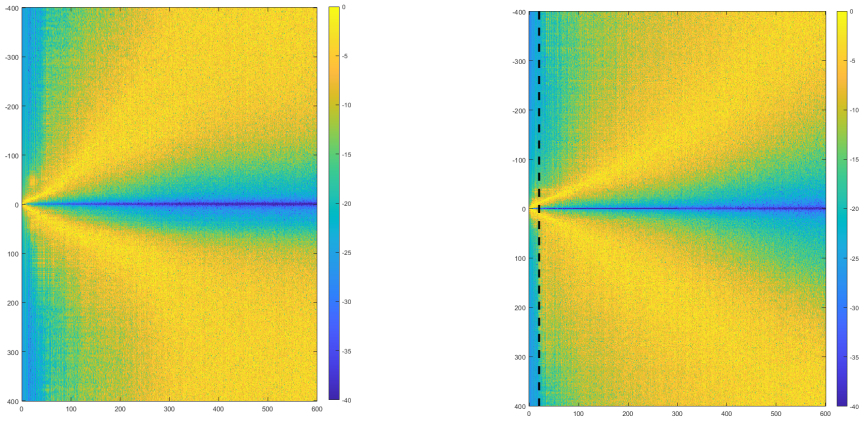

(a) PSD of V

(b) Threshold selection

Figure 3.6: PSD obtained by using fast Fourier transform on V. The x-axis is the temporal dimension, and the y-axis is the frequency in Hertz (HZ).

As observed from figure 3.6, low frequency is associated with high-energy singular vectors and high frequency with low-energy singular vectors. The reason is that high-energy singular vectors are associated with tissue that has high temporal coherence because of the slow movement and the opposite for blood flow.

The threshold selection can be based on the central frequency. For example, frequencies lower than a certain value can be considered as tissue and discarded. The extracted central frequency of PSD of V is shown in Figure 3.7. The central frequency is calculated by averaging the minimum frequency value and the maximum frequency value of a certain frequency amplitude of each column. The central frequency curve is then smoothed by mean envelope extraction (Matlab function envelope) or other smoothing method.

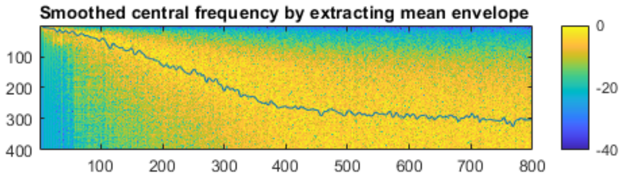

Figure 3.7: Central frequency of PSD of V

So far, methods based on singular values, and spatial/temporal singular vectors to decide the threshold has been introduced. These methods can be applied to global SVD clutter filtering, or block-wise SVD clutter filtering [4, 7]. However, subspaces for tissue and blood flow principle components are not always distinct after SVD [32]. Overlapped subspaces demonstration and explanation can be found in chapter 4.1.3.

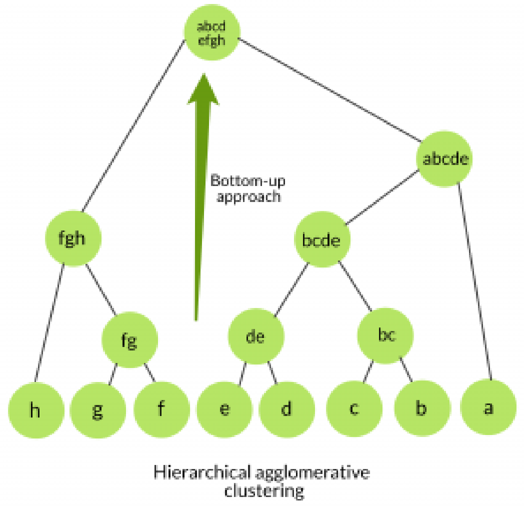

Figure 3.8: Hierarchical agglomerative clustering example [6].

3.2.5 Clustering

Besides choosing the threshold criteria by discovering separated subspaces from spatial similarity matrices of **U** and PSD of **V** as explained in section 3.2.3 and 3.2.4, clustering methods can also be used to group singular component vectors based on similarities. Hierarchical agglomerative clustering is the most common clustering method based on similarities. It works by iteratively merging clusters with minimal distances in a bottom-up approach as Figure 3.8 shown. Different algorithms can be used to calculate the distance between clusters. Ward's method which calculates the inner squared distance (minimum variance algorithm) is chosen in this thesis. The number of clustering is not restrictive to be a certain number. It depends on different datasets and used methods.

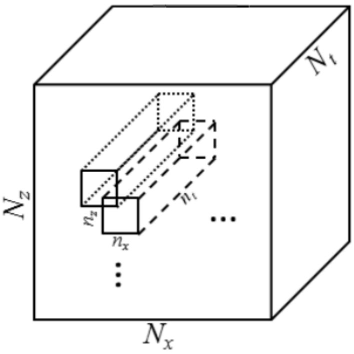

Figure 3.9: Schematic plot of processing 3D planewave data into overlapped blocks [7].

3.2.6 Block-wish approach

So far, all decompositions are based on global SVD clutter filtering. One of the challenges of taking a global threshold is that the threshold is not always applicable to all fields. It can be the case that some tissue motion in the near field still remains while some small blood vessels in the far field are overly removed. This can be addressed by applying overlapped block decomposition approach. This block-wise approach works by decomposing 3D planewave data into overlapped small blocks. After extracting the small blocks, the clutter filtering process works the same as for global SVD clutter filtering as explained in the previous section 3.2 in Figure 3.2.

Song *et al.* [7] has experimented with block-wise local SVD clutter filtering technique and they have found that for some datasets this approach can improve the separation of the tissue, blood flow, and noise, and also some small vessel PDIs can be further improved due to the redundant nature of overlapped block decomposition.

3.3 Robust PCA-based clutter filtering technique

Robust PCA-based clutter filtering is another method to decompose the mixed signal matrix. It assumes that the beamformed data **X** can be decomposed into one low-rank matrix containing tissue motion and one sparse matrix containing blood flow. It improves clutter filtering on the aspect of microvessel sparsity [17]. It aims to recover a low-rank matrix and a sparse matrix from a corrupted measurement. Here the rank of **L** and the cardinality of **S** are unknown. $\mathbf{X} \in \mathbb{R}^{n_x n_z \times n_x}$, $\mathbf{L} \in \mathbb{R}^{n_x n_z \times n_x}$, $\mathbf{S} \in \mathbb{R}^{n_x n_z \times n_x}$.

$$\mathbf{X} = \mathbf{L} + \mathbf{S} \tag{3.7}$$

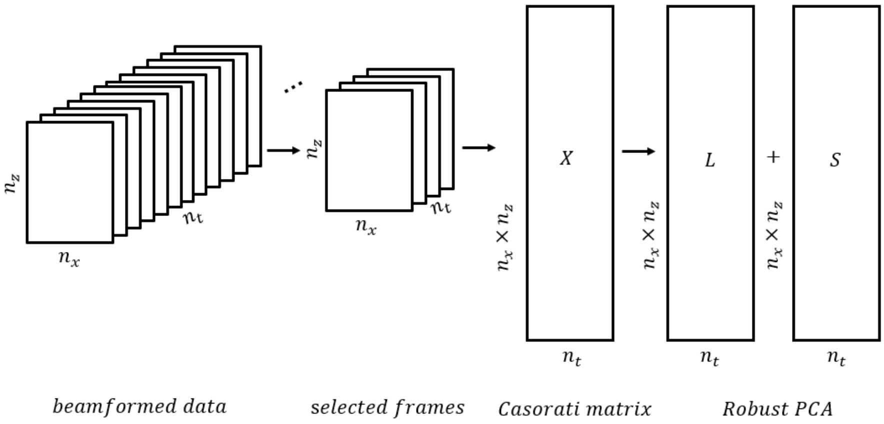

Figure 3.10: Robust PCA principle

The low-rank matrix **L** and sparse matrix **S** can be recovered by solving the principle component pursuit convex program by minimizing the weighted combination of the nuclear norm of **L** and of the ℓ_1 norm of **S** [33] as 3.8:

$$\begin{aligned} \text{minimize } & \|\mathbf{L}\|_* + \lambda \|\mathbf{S}\|_1 \\ \text{subject to } & \mathbf{X} = \mathbf{L} + \mathbf{S} \end{aligned} \tag{3.8}$$

where the nuclear norm $\|\mathbf{L}\|_*$ is the sum of its singular values and the ℓ_1 norm $\|\mathbf{S}\|_1$ is the sum of its absolute vector values. λ is the regularization parameter that controls the trade-off between the low rank and sparsity.

This convex program can be solved by many algorithms. Previous methods include using interior point methods [34], repeatedly shrinking the singular values of an appropriate matrix [35], or using Nesterov's optimal first-order algorithm for smooth minimization [36]. The alternating direction method of multipliers (ADMM) algorithm is a classical way to solve this convex program which can achieve much higher accuracy in fewer iterations [37]:

$$\mathcal{L}(L, S, Y, \mu) = \|L\|_* + \lambda \|S\|_1 + \langle Y, X - L - S \rangle + \frac{\mu}{2} \|X - L - S\|_F^2 \tag{3.9}$$

L is updated as:

$$L_{N+1} = D_{\frac{1}{\mu}} \left(X - S_N + \mu^{-1} Y_N \right), \tag{3.10}$$

where $D_\tau(X) = U S_\tau(\Sigma) V^*$. **S** is updated as:

$$S_{N+1} = S_{\frac{\lambda}{\mu}}\left(X - L_{N+1} + \mu^{-1}Y_N\right), \tag{3.11}$$

where $D_\tau(X) = US_\tau(\Sigma)V^*$.

$S_\tau[x] = \mathrm{sgn}(x)\max(|x|-\tau, 0)$ is the shrinkage operator and $D_\tau(X) = US_\tau(\Sigma)V^*$ denotes the singular value thresholding operator. $\mathcal{L}$ is first minimized by updating L with fixing S, and then minimized by updating S with fixing L. Finally, the Lagrange multiplier is updated based on the residual $X - L_N - S_N$.

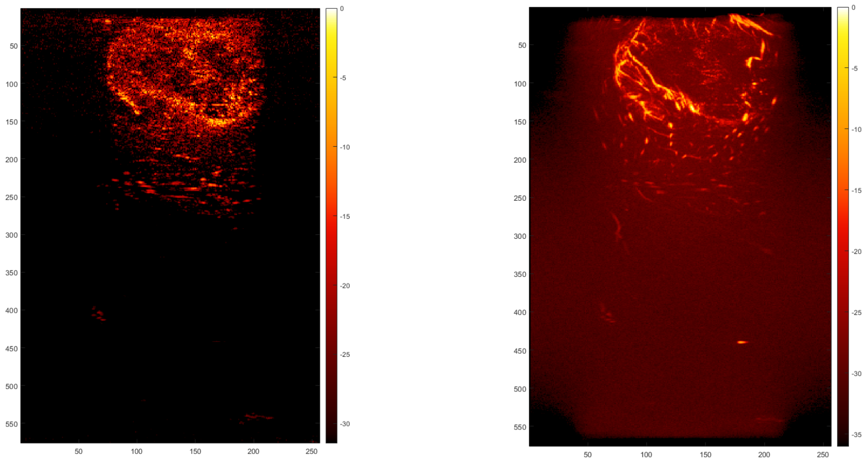

(a) low-rank matrix

(b) sparse matrix

Figure 3.11: Visualization of Robust PCA decomposition. The size of both images is $n_x \times n_z$. The image intensity is in dB.

Figure 3.11 compares low-rank matrix and sparse matrix decomposition from Robust PCA. The ensemble size is 400, λ is set as 0.002, and μ is set as 5. There is most tissue clutter in 3.11a but most blood vessels in 3.11b. The matrix decomposition is largely affected by the values of λ and μ. The parameter value selection will be further discussed in Chapter 4.

3.4 ICA-based clutter filtering technique

ICA can reveal their information by separating the mixed signals into independent components with the assumption that independent sources have non-Gaussian distribution [38].

3.4.1 ICA principles

Data model The mixing model can be written as [39]:

$$\mathbf{X} = \mathbf{AS}, \tag{3.12}$$

Where $\mathbf{X}$ is a Casorati matrix with a size of $n_t \times n_x n_z$, $\mathbf{A}$ has a size of $n_t \times n$, $\mathbf{S}$ has a size of $n \times n_x n_z$, and n is the number of independent components. The assumption is that there are several sources with a certain spatial signature but their intensity varies over time. The vectorized source images are s_n and their temporal variation is expressed by the rows of the mixing matrix, meaning that a_{jn} express the intensity of the j_{th} source at time points n_t.

x_j can be written as the summation of the product of independent components s_n and mixing matrices a_{jn}, where a_{jn} gives the weighting of how s_n is combined to construct x_j.

$$x_j = a_{j1}s_1 + a_{j2}s_2 + \ldots + a_{jn}s_n, \text{ for all } j. \tag{3.13}$$

After estimating $\mathbf{A}$, $\mathbf{S}$ can be obtained by:

$$\mathbf{S} = \mathbf{A}^{\mathbf{-1}}\mathbf{X} \tag{3.14}$$

Assumption and restriction The source signals are independent of each other, and the distribution in each source signal is non-Gaussian, which is the fundamental assumption and restriction for ICA. Gaussian variables (normal distribution with zero mean and unit variance) make ICA impossible. Assuming that s_i is Gaussian and $\mathbf{A}$ is orthogonal, then x_i is Gaussian. The joint density is symmetric and, therefore, does not contain information on the directions of the columns of the mixing matrix $\mathbf{A}$. Thus, $\mathbf{A}$ cannot be estimated. To separate independent signals from their mixtures, it is important to ensure that the linear signal transformation is as non-Gaussian as possible.

Maximizing non-Gaussianity can yield one of the independent components. Kurtosis, negentropy, and the minimization of mutual information can be quantitative measures of non-Gaussianity [39]. Kurtosis is a classic measure defined by the equation 3.15. As y is assumed of unit variance, thus $3\left(E\left\{y^2\right\}\right)^2$ simplifies to 3. If $\text{kurt}(y)$ is zero, the random variable is Gaussian. The absolute value of kurtosis can be used as a measure of non-Gaussianity.

$$\text{kurt}(y) = E\left\{y^4\right\} - 3\left(E\left\{y^2\right\}\right)^2 = E\left\{y^4\right\} - 3 \tag{3.15}$$

Pre-processing The pre-processing steps consist of centering and pre-whitening the data [39]. Centering processing means that data is centered by subtracting the mean vector. After the estimation of the mixing matrix, the mean can be added back to the centered estimates of $\mathbf{S}$.

Prewhitening is to transform the observed vector $\mathbf{x}$ linearly so that the new vector is white, which means that the components are uncorrelated (covariance is zero) and they have unity variances ($E\left\{\tilde{\mathbf{x}}\tilde{\mathbf{x}}^T\right\} = \mathbf{I}$). The whitening processing can reduce the number of parameters to be estimated.

For the steps of pre-whitening, first, take eigenvalue decomposition of the covariance of $\mathbf{X}$:

$$C = E\left\{\mathbf{x}\mathbf{x}^T\right\} = \mathbf{EDE^T}, \tag{3.16}$$

where $\mathbf{E}$ is the orthogonal eigenvector matrices of $\mathbf{C}$ and $\mathbf{D}$ is the diagonal eigenvalue matrices. Then, pre-whitened data is $\tilde{\mathbf{x}} = \mathbf{ED^{-\frac{1}{2}}E^TX}$. The mixing matrix $\mathbf{A}$ can be transformed into a new matrix $\tilde{\mathbf{A}}$:

$$\tilde{\mathbf{x}} = \mathbf{ED^{-\frac{1}{2}}E^TX} = \mathbf{ED}^{-1/2}\mathbf{E}^T\mathbf{As} = \tilde{\mathbf{A}}\mathbf{s} \tag{3.17}$$

Now the components have unity variances and have zero covariance after whitening:

$$E\left\{\tilde{\mathbf{x}}\tilde{\mathbf{x}}^T\right\} = \tilde{\mathbf{A}}E\left\{\mathbf{s}\mathbf{s}^T\right\}\tilde{\mathbf{A}}^T = \tilde{\mathbf{A}}\tilde{\mathbf{A}}^T = \mathbf{I} \tag{3.18}$$

$$E\left\{\tilde{\mathbf{x}}\tilde{\mathbf{x}}^T\right\} - E\left\{\tilde{\mathbf{x}}\right\}E\left\{\tilde{\mathbf{x}}\right\} = 0 \tag{3.19}$$

ICA algorithm There are many ICA algorithms for decomposing the mixing matrix $\mathbf{X}$. The Fast ICA algorithm is a fixed-point optimization method that optimizes over a contrast function, usually defined by an approximation of negentropy or excess kurtosis. The contrast functions are defined as statistical functions capable of separating or extracting independent sources from a linear mixture [40]. Robust ICA is based on the normalized kurtosis contrast function, which is optimized using a computationally efficient iterative technique [41]. The main advantages of Robust ICA are its high convergence rate and the ability to process both real- and complex-valued signals. In this thesis, I adopted the Robust ICA algorithm, and the MATLAB package created by V. Zarzoso and P. Comon [41] can be found at this link [42].

3.4.2 The application on functional ultrasound imaging

The observation of mixtures $\mathbf{X}$ can be considered as the linear combined mixtures of tissue clutter $\mathbf{C}$, blood flow $\mathbf{B}$, and other noise $\mathbf{N}$:

$$\mathbf{X} = \mathbf{C} + \mathbf{B} + \mathbf{N} \tag{3.20}$$

where $\mathbf{X}$, $\mathbf{C}$, $\mathbf{B}$, and $\mathbf{N}$ all have a size of $(n_t, n_z n_x)$.

A direct way to apply ICA clutter filtering is to decompose the Casorati matrix $\mathbf{X}$ with size $(n_z \times n_x, n_t)$ into independent components ($\mathbf{X} = \mathbf{AS}$), as shown in Figure 3.12. ICA works by solving the mixing matrix $\mathbf{A}$, and $\mathbf{S} = \mathbf{A^{-1}X}$. Another approach is to combine SVD and ICA clutter filtering [18], as illustrated in Figure 3.13. Before applying ICA to $\mathbf{X}$, an additional SVD step is performed to remove $\mathbf{N}$. The noise-removed $\mathbf{X}$ is then divided into smaller time windows to apply ICA clutter filtering.

After extracting the independent components, another challenge is to select components that correspond only to blood flow. Wahyulaksana *et al.* [18] proposed a sorting method based on kurtosis measurement values. They believed that blood vessels are

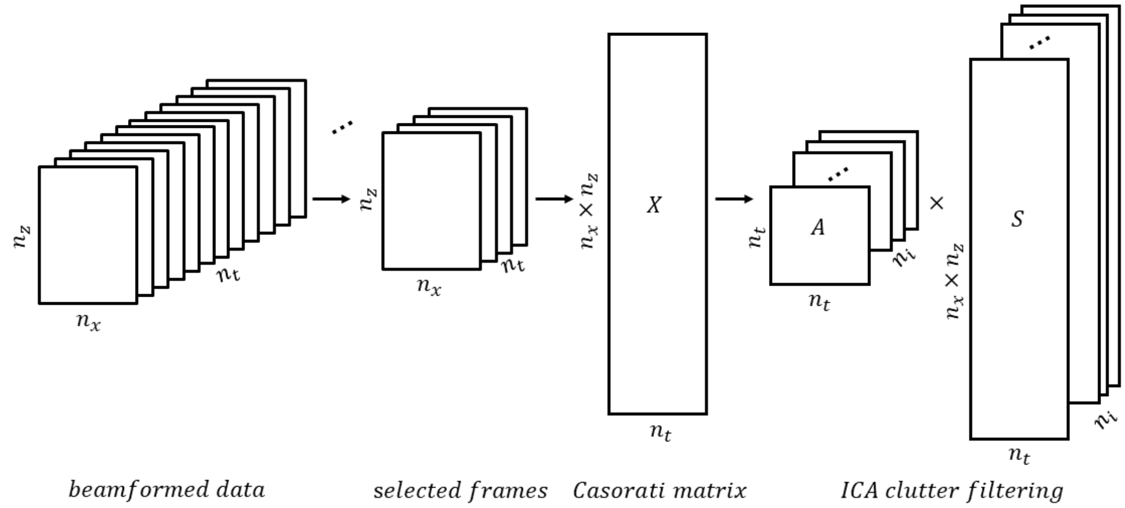

Figure 3.12: A direct way of ICA clutter filtering

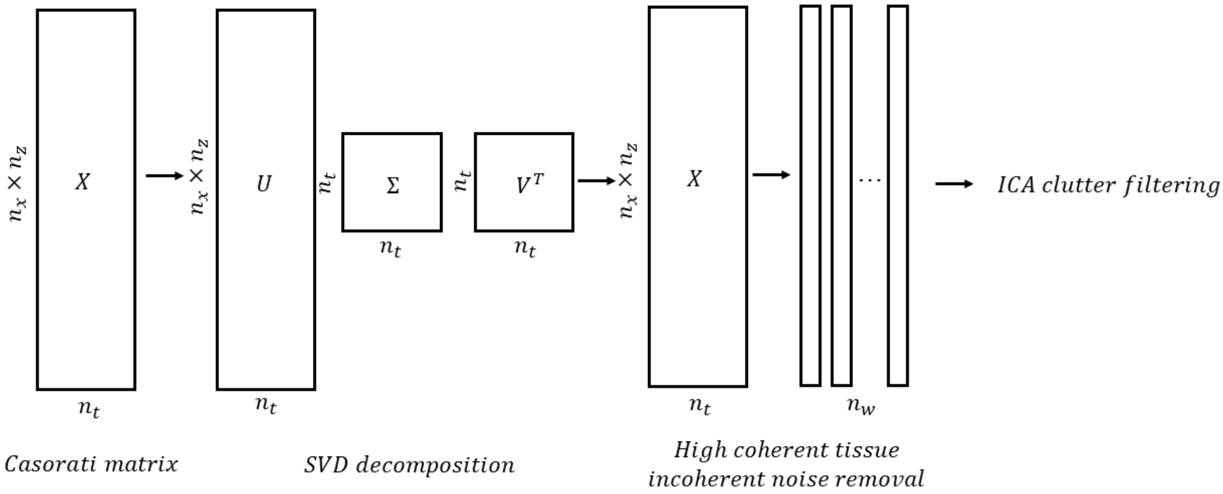

Figure 3.13: SVD and ICA combined clutter filtering

sparser and thus have higher kurtosis values than tissue. Tierney *et al.* [19] used sorted independent components based on correlation coefficients computed between reconstructed power Doppler images created with each individual independent component and a power Doppler image created with all components. They asserted that a component that produces a high correlation coefficient likely contains tissue, while a component that produces a low correlation coefficient contains blood. In this thesis, the selection method employed is to apply hierarchical agglomerative clustering to independent sources to separate tissue clusters and blood flow clusters. This method does not require independent component ordering and has been found to be effective for our ultrasound data compared to kurtosis-based ordering and correlation-based ordering. The results and analysis can be found in Chapter 4.

3.5 Fair comparison methods

Making fair comparisons is important, especially among results from different clutter filtering techniques. There are following aspects to consider:

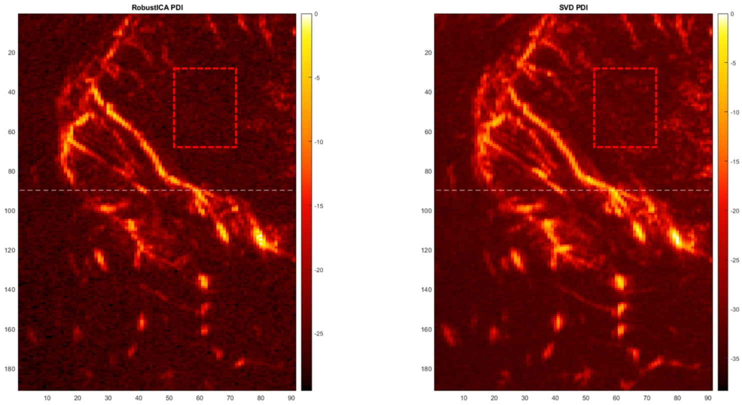

Figure 3.14: The comparison between Robust PCA clutter filtering and SVD clutter filtering. The dynamic range is set as the mean value of all pixels in the selected background area (red rectangular area).

1. Stack of frames. The stack of frames used to reconstruct images needs to be the same, including the starting point of the frames and the ensemble length. This ensures that their spatial and temporal information are the same.

2. Image mean contrast intensity. Image mean contrast intensity needs to be on the same level. This can be done by setting the limit of the dynamic range to the mean value of all pixels in the background area. The background area contains almost no tissue or blood flow. For example, when comparing images filtered by Robust PCA and SVD as Figure 3.14 shows, the mean value of all pixels in the selected background area (red rectangular area) is calculated and set as the dynamic range limit so the image mean contrast visualization is similar.

3. Proper threshold choosing. Thresholds need to be carefully selected to reconstruct an ultrasound image. For example, When comparing different clutter filtering techniques with SVD clutter filtering, a too-high or too-low threshold can lead to a wrong judgment of image quality. For Robust PCA clutter filtering, improper λ and μ value selection could lead to the filtered image being too sparse or too low-rank, thus affecting the image quality. For ICA clutter filtering, inappropriate independent component sorting and clustering could result in revealing not much blood flow information or too much tissue clutter.

4. Quantitative metrics. Quantitative metrics are objective numerical measurements used to evaluate image quality. They serve as ancillary tools for direct image observations. SNR and CNR are commonly used in evaluating μDoppler images. SNR measures the ratio of blood flow intensity in the region of interest and the

standard deviation of the background noise. CNR measures the ratio of the difference between blood flow intensity in the region of interest and the standard deviation of background noise. However, when using quantitative metrics, it remains crucial to keep a critical approach when using these measurements and ensure that the measurements are fair and reliable.

Results

4

4.1 SVD clutter filtering

4.1.1 The effect of probe movement on threshold choices

Probe movement means that the area scanned by the probe changes over time. Understanding how movement influences threshold choices is essential to provide guidance on operating probe scanning and determining appropriate thresholds.

Threshold choices for separating tissue and blood flow between stationary and moving datasets using an ensemble size of 200 and 400 are compared in Figure 4.1a and 4.1b. Thresholds were determined using an automated SVD clutter filter based on spatial similarity matrices (Chapter 3.2.3), as proposed and tested by Baranger *et al.* [14]. Their method is widely used and generally known to produce good results. In this part, we consider thresholds determined by this method as optimal thresholds. The focus of this analysis is on the threshold results, rather than the specific clutter filtering methods employed.

In both figures, thresholds are compared for a stationary dataset and a moving dataset, both obtained from the same patient's brain during surgery. The scanned areas in these datasets are close to each other, ensuring that probe movement could be the only influencing factor for the threshold choices.

The common observation in both figures is that the optimal thresholds exhibit relative stability over time for the stationary dataset, while they show significant variation for the moving dataset. In the left-side figure, which compares the thresholds with an ensemble size of 200, the variance of threshold choices is 2.5299 for the stationary dataset, whereas it increases to 76.5161 for the moving dataset. This difference in variance becomes even more pronounced for an ensemble size of 400, which covers a wider time range. The variance of threshold choices for the stationary dataset is 2.1195, whereas for the moving dataset, it rises to 122.2126.

The probe movement information can also be revealed from the correlation matrix. The correlation matrix is calculated as:

$$\rho(X, X) = \frac{1}{n_t - 1} \sum_{i=1}^{n_t} \left(\frac{X_i - \mu_X}{\sigma_X} \right) \left(\frac{X_i - \mu_X}{\sigma_X} \right), \tag{4.1}$$

where X is the Casorati matrix, μ_X is the column mean, and σ_X is the column standard deviation. It has the same calculation as Equation 3.6. It represents the correlation values among the columns of X containing the spatial information from different frames.

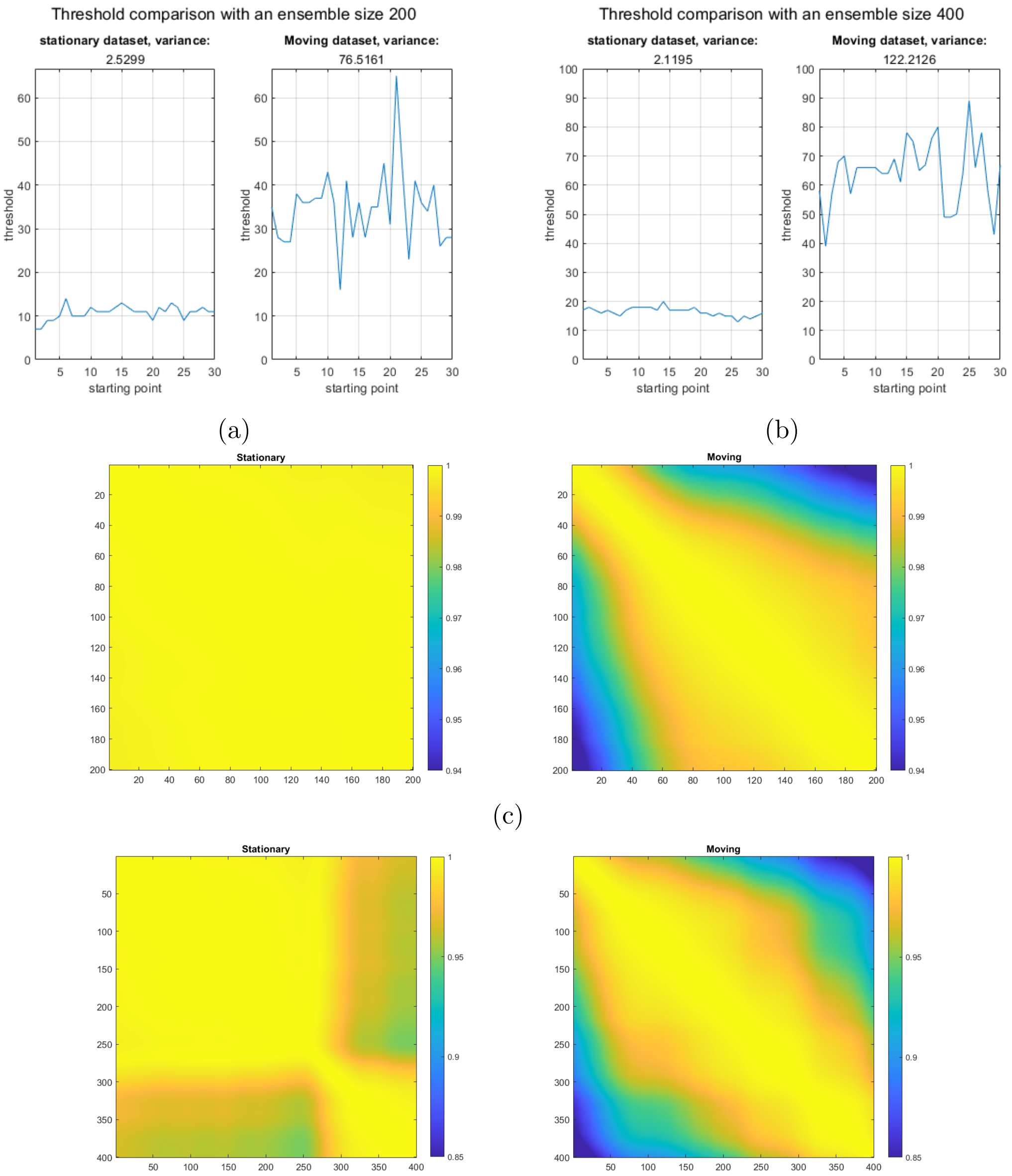

(a) (b)

(c)

(d)

Figure 4.1: (a)(b) Threshold comparisons between stationary and moving datasets with an ensemble size of 200 and 400 using an automated SVD clutter filer. The x-asix represents different stacks of frames index of the same datasets. (c)(d) The correlation matrix of neighboring pixels calculated as Equation 4.1 is of dimension 200×200 and 400×400.

It is symmetric and non-negative. Figure 4.1c presents the correlation matrix of a stationary dataset and a moving dataset of dimension 200×200.

For the correlation matrix of the stationary dataset, the magnitude of the correlation values is very high as observed. This indicates that the spatial information of each frame is highly correlated with each other. This observation also aligns with the stable threshold criteria shown in Figure 4.1a. On the other hand, when observing the correlation matrix of the moving dataset, very high correlation values concentrate around the diagonal area. This reveals that neighboring frames highly resemble each other, while for frames further apart, the spatial coherence decreases, resulting in lower correlation. As 200 frames take only $250ms$, the lowest correlation still has a high value.

The same analysis can be applied to Figure 4.1d, which displays the correlation matrix of a stationary dataset and a moving dataset of dimension 400×400. Overall, the correlation values in the off-diagonal area are lower compared to those in Figure 4.1c of dimension 200×200. This is evident from the darker colors in the off-diagonal area and the narrower width of the bright diagonal area. This indicates that with more frames involved, the difference between the very first and very last frames becomes larger. This makes sense as the total displacement between the first and last frame is larger. Nevertheless, the correlation of the stationary dataset still exhibits higher overall values than the moving dataset. In the stationary dataset, the areas with lower values could indicate a small shift in the tissue, for example, during a heartbeat.

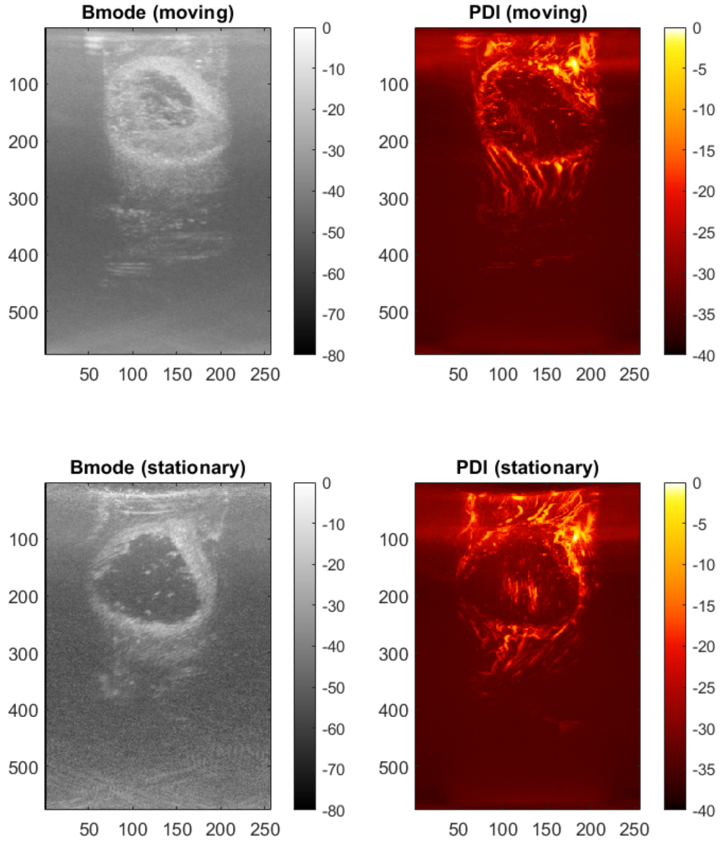

Figure 4.2: Comparison between B-mode images and reconstructed PDIs of a stationary dataset and moving dataset with the dimension 800×800 for a stack of frames from 4900 to 5699.

Besides comparing thresholds and frame correlation on different moving and stationary datasets with different scan areas, it is also interesting to discover these differences for datasets with similar scan areas. Figure 4.2 displays two sets of B-mode and SVD-

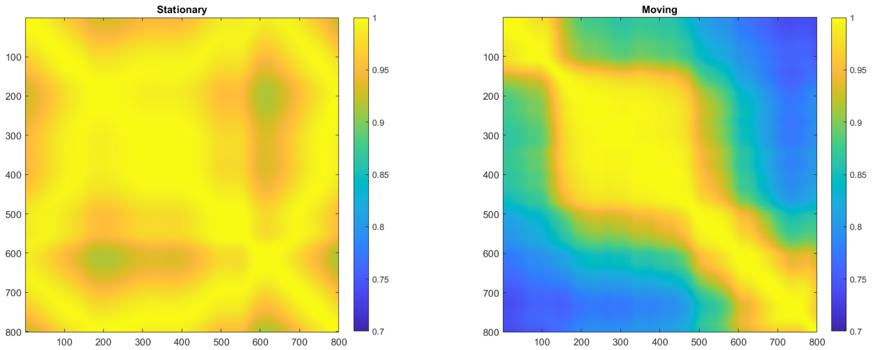

Figure 4.3: Comparison between correlation matrices of a stationary dataset (left-side figure) and moving dataset (right-side figure) with the dimension 800 × 800 for a stack of frames from 4900 to 5699.

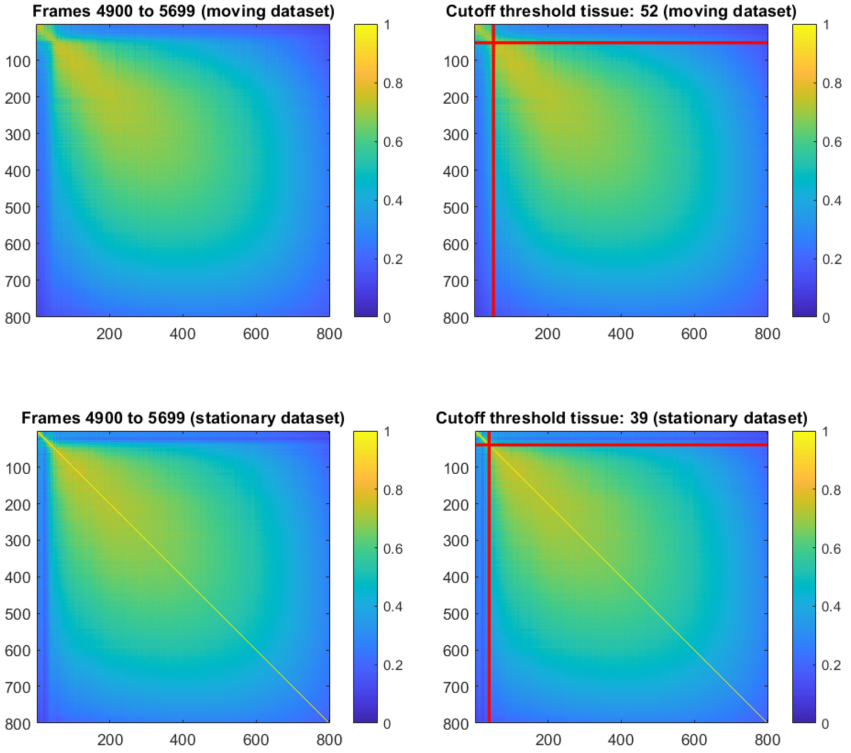

Figure 4.4: Comparison between spatial similarity matrices C of a stationary dataset and moving dataset with the dimension 800 × 800 for a stack of frames from 4900 to 5699.

filtered power Doppler images reconstructed from different datasets. Their scanned areas are very close to each other, therefore it is considered that tissue and blood flow characteristics are very similar for both sets. Their movement characteristics are shown in Figure 4.3 where the frames are more correlated in a stationary dataset than in a moving dataset. The movement information can also be discovered from spatial similarity matrices, as shown in Figure 4.4. The subspace squares display more distinguishable in a stationary dataset than in a moving dataset.

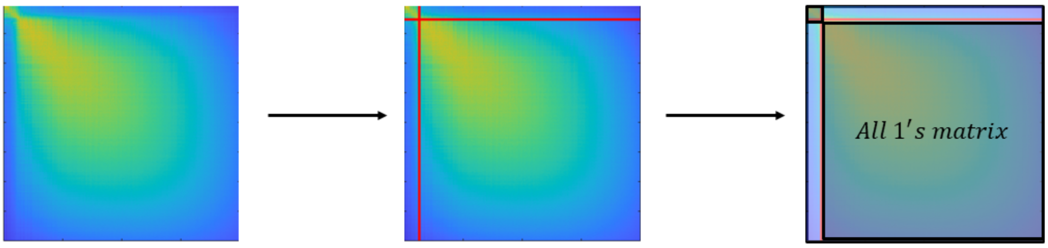

Correlation matrix (C)

Correlation matrix with a threshold

Correlation coefficients between the juxtaposed matrix and C

Figure 4.5: Calculation of correlation coefficients: the correlation coefficients are computed by correlating juxtaposed matrices filled in all 1's with the spatial similarity matrix.

Tissue and blood flow subspaces are not always in a square shape and correlation coefficients are computed to evaluate the fit of data distribution in spatial similarity matrices segmented by a threshold. The calculation method is outlined in Figure 4.5. Following the threshold selection for separating tissue and blood flow, the juxtaposed matrices (matrices represented by dark color) filled with all ones are correlated with the spatial similarity matrices to derive the correlation coefficients.

The correlation coefficients computed between spatial similarity matrices and unit juxtaposed matrices of size 800 is presented in Table 4.1, with varying starting points of the frames. The objective is to identify common findings regarding the correlation of their own respective subspaces across different frames. As observed in the table, the correlation coefficients consistently indicate higher values for stationary datasets compared to moving datasets, regardless of the spatial content of the frames. This suggests that tissue and blood flow subspaces exhibit greater distinguishability and correlation with their respective subspaces in stationary datasets compared to moving datasets.

Ensemble size	Start Point	Dataset Type	Correlation coefficients
800	1400	Moving	0.2438
		Stationary	0.3086
	2200	Moving	0.2946
		Stationary	0.4175
	3000	Moving	0.3682
		Stationary	0.4157
	3800	Moving	0.4002
		Stationary	0.4344
	4600	Moving	0.3901
		Stationary	0.3928

Table 4.1: Comparison of correlation coefficients between spatial similarity matrices and unit juxtaposed matrices (matrices with a dark area) of a stationary dataset and moving dataset with an ensemble size of 800.

4.1.2 Trade-off choices between ensemble sizes, threshold selections, and image intensity

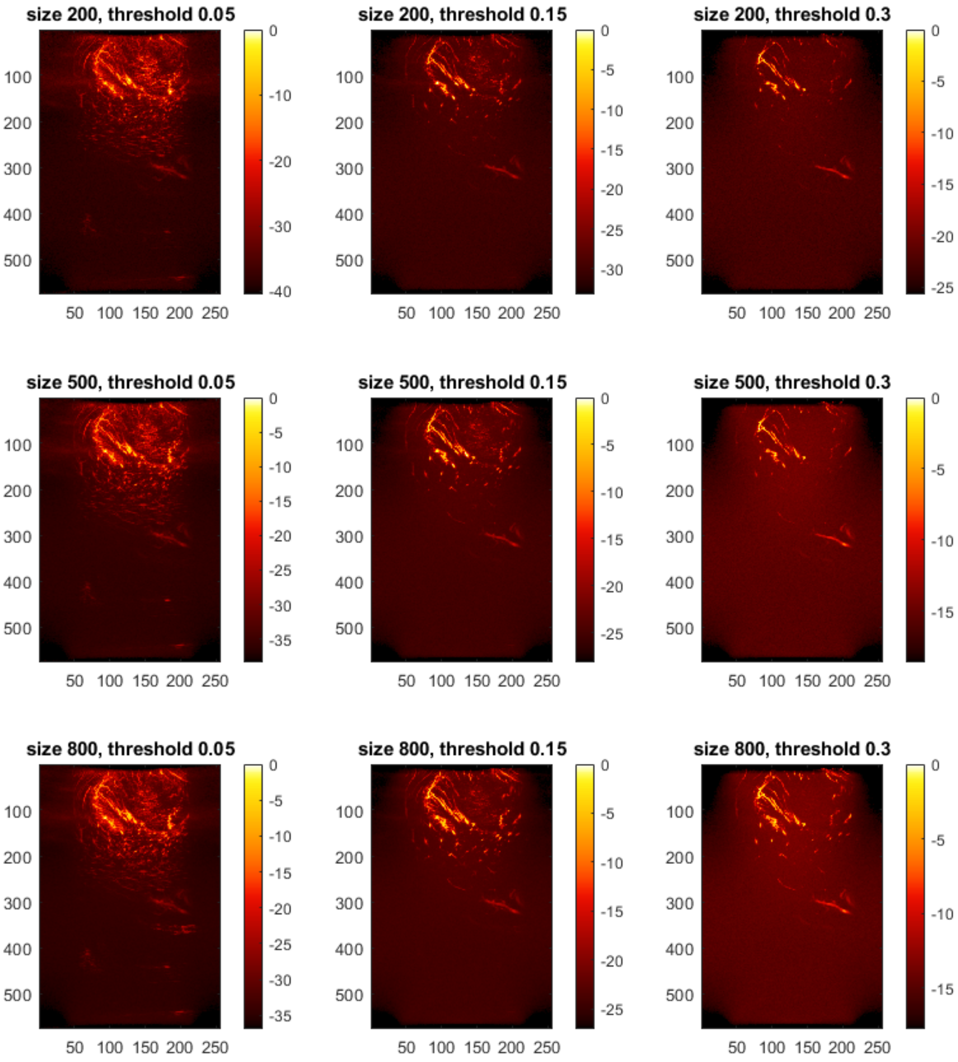

Figure 4.6: Comparisons of ensemble sizes and threshold choices: vertical axis - same ensemble sizes and different thresholds, horizontal axis - same thresholds and different ensemble sizes.

SVD takes advantage of the large ensemble length achieved by the ultrafast Doppler technique. A large ensemble size results in high power Doppler contrast. However, it also implies that the ensemble covers a longer time duration. This can be vulnerable, particularly in the case of moving datasets, as the image content changes over time. Consequently, when images are integrated over temporal dimension, vessels that are not in the same location are compounded, thereby making it seem that vessels are connected even though they can be far apart in reality.

Figure 4.6 compares the image quality of different ensemble sizes (200, 500, and 800) and threshold choices (5%, 15%, and 30%) for a moving dataset. From empirical research, the 5% threshold is much lower than the optimal threshold to remove all tissue clutter and the 30% threshold is way higher that some blood flow information could disappear. The colorbar limit of each image is adjusted based on the background intensity as a reference. When examining the comparisons horizontally, which means considering the same ensemble size but different thresholds, several observations can be made: with a threshold of 5%, indicating that the first 5% of singular components are discarded, a significant amount of tissue motion appears in the upper middle area compared to thresholds of 15% and 30%. When using a threshold of 30%, it becomes evident that some blood vessel structures are not visible on the right side of the image. This suggests that the high threshold value leads to the discarding of certain blood flow information. By analyzing these comparisons, we gain a better understanding of the impact of different threshold choices on the visualization of tissue motion and blood flow information: a low threshold can result in the retention of tissue motion, while a high threshold can lead to the exclusion of important blood flow information.

When observing the comparisons vertically, which means considering the same thresholds but different ensemble sizes, the image mean contrast becomes higher as the ensemble length increases. Figure 4.7 provides a zoomed-in view of SVD-filtered images with a threshold of 15% and ensemble sizes of 200 and 800, respectively. It is evident that the left-side figure exhibits a greater amount of blood vessels overlapping each other compared to the right-side figure. This phenomenon indicates that during the time range covered by the ensemble length of 800, the content of blood vessels changes, resulting in the visualization of overlapping vasculature.

A longer ensemble length improves image intensity but also introduces the issue of overlapping blood vessel information. Trade-off choices regarding ensemble length need to be made to balance image intensity and the occurrence of overlapping information. Additionally, it is crucial to make appropriate threshold choices to exclude excessive tissue motion while preserving essential blood flow information.

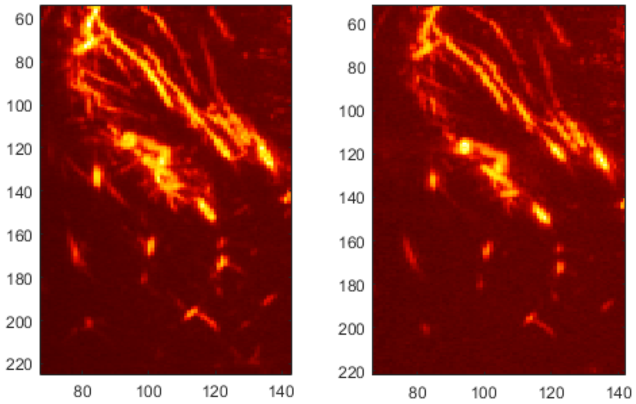

Figure 4.7: Image comparison of the upper-left region: ensemble size 800 (left-side figure) and 200 (right-side figure) with the same threshold 15% (zoomed-in view).

4.1.3 Overlapped subspaces on eigen-domain

SVD clutter filtering performs well in the case of slow tissue motion and fast blood flow as their power spectrum and spatial information are more separately distributed. They can be expressed by different subspaces, but they may be usually overlapped. From the perspective of the power spectral density (PSD) of V, their frequency spectra can overlap. Figure 4.8 is PSD of V on a stationary dataset with an ensemble size 600. In the case of a stationary dataset where the probe does not move, the overlap between tissue and blood flow subspaces can be attributed to the movement of tissue and blood flow. The 20th component is selected as the threshold to be able to distinguish tissue and blood flow the most. In this figure, two black-dashed lines represent the 10th and 200th components, which are assumed to belong to tissue and blood flow respectively.

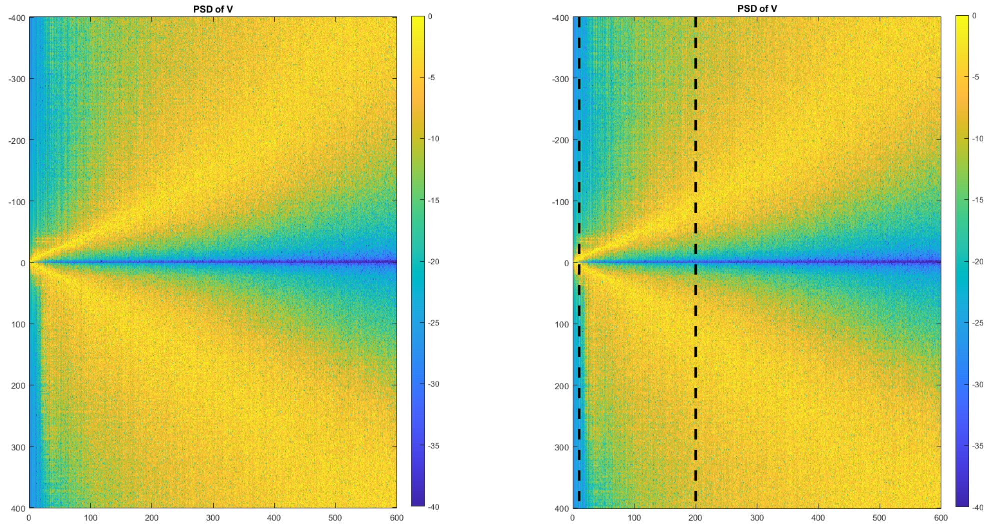

Figure 4.8: PSD of V: Fourier transform of temporal singular vectors. Two dashed lines represent the 10^{th} and 200^{th} components respectively.

When their frequencies are extracted, as shown in Figure 4.9, there is an overlap at a frequency of 30Hz. If frequency amplitudes below -25dB are considered insignificant, the frequency range of the 10th component is between 0Hz and 50Hz, while the frequency range of the 200th component is between 5Hz and 400Hz. The bandwidths overlap between 5Hz and 50Hz.

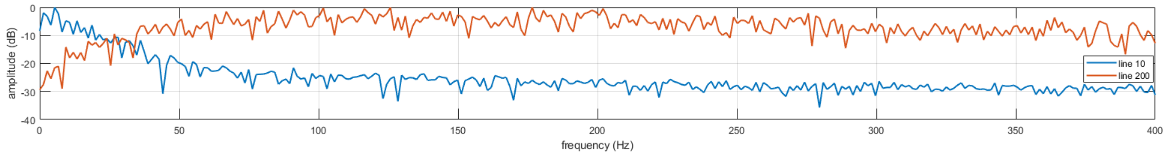

Figure 4.9: frequency spectra of the 10^{th} and 200^{th} singular component.

The overlapped frequency spectra can be observed from the visualizations of the 10th and 200th components, as shown in Figure 4.10. The left image primarily represents tissue motion, but there are certain areas that appear to belong to blood vessels. For instance, a few high-intensity blood vessels can be observed in the orange squares. The reason these bright and intense areas could be identified as blood flow is that they are also visible in the visualization of the 200th component, which most likely corresponds to blood flow.

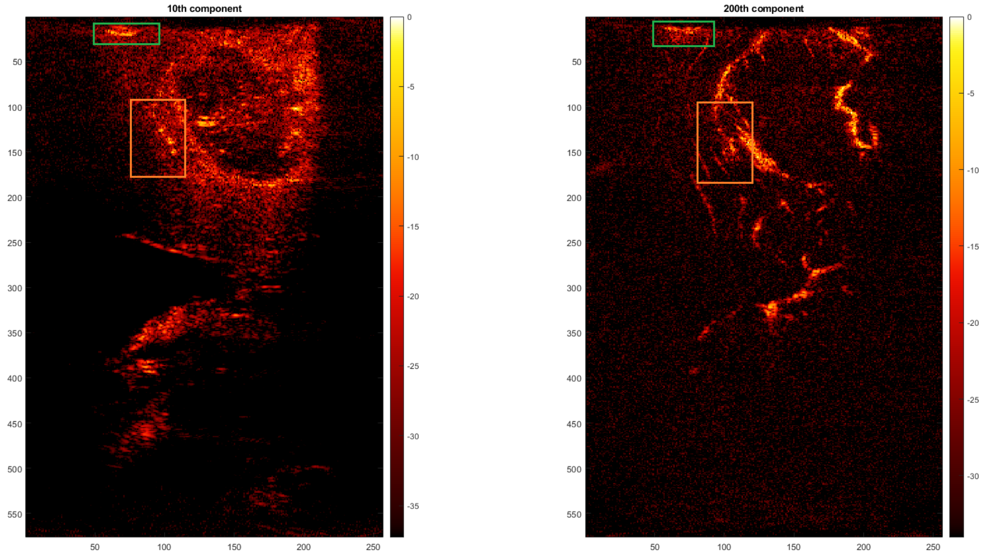

Figure 4.10: Visualization of the single 10^{th} component (left figure) and the single 200^{th} component (right figure). It is hard to define rigorously whether or not a feature in an image is a blood vessel and this is generally done in the field by visual inspection.

After summing the PSD of the tissue subspace (first 20 components) and the blood flow subspace (20-600 components), the frequency distribution is shown in Figure 4.11. The same analysis methodology used to analyze the frequency spectra of the 10th and 200th components can be applied here. The frequency spectra of the tissue subspace range from 0Hz to 40Hz, while the frequency spectra of the blood flow subspace range from 15Hz to 400Hz if the frequency amplitude greater than -15dB is considered. The overlapped frequency spectra are between 15Hz and 40Hz.

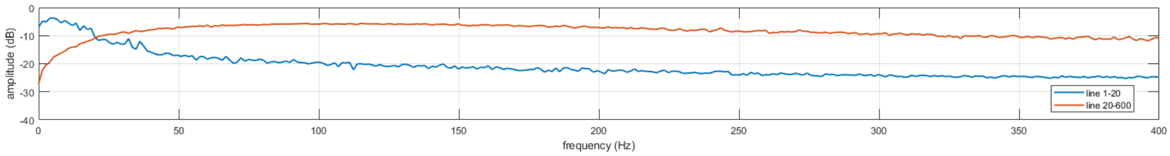

Figure 4.11: Frequency spectra of the first 20 components and 20-600 components.

After summing the power over tissue subspace and blood flow subspace to reconstruct PDIs, as shown in Figure 4.12, it can be observed that there is tissue motion present in the PDI from the blood flow subspace (right side figure), and there are blood vessels visible in the PDI from the tissue subspace (left side figure) that should not be observed. This observation shows that there is an overlap between the subspaces of tissue motion and blood flow, leading to incomplete separation of the subspaces.

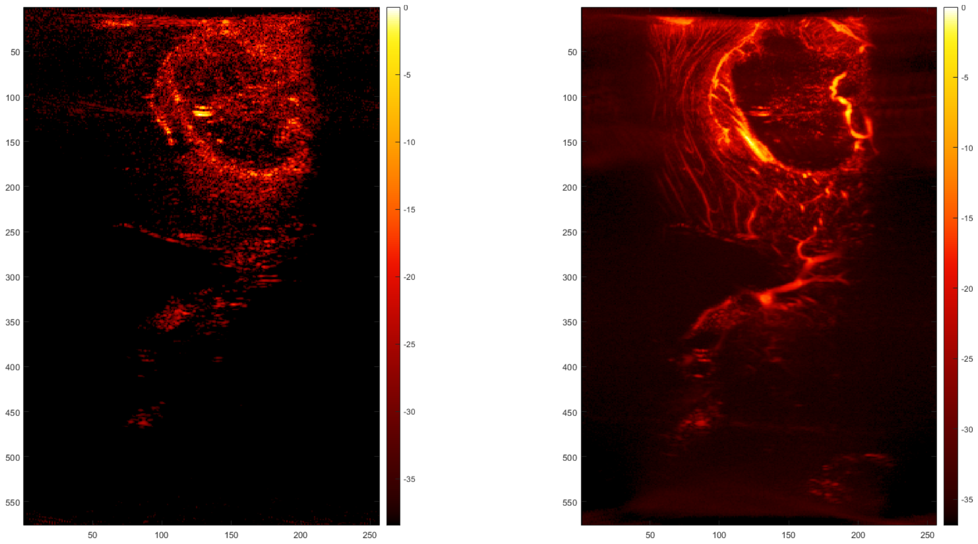

Figure 4.12: PDIs reconstructed by first 20 components (left figure) and 20-200 components (right figure).

Overlapping can also be observed in the similarity matrix of U, which represents the correlation among columns of the spatial singular vectors. For instance, Figure 4.13 compares the similarity matrices of a moving dataset with ensemble sizes of 100 and 800. Since the sampling frequency F_s is 800 samples/second, an ensemble size of 800 covers a time course of 1 second, while an ensemble size of 100 covers a time course of 0.125 seconds. Distinct subspaces are more pronounced in the left figure with an ensemble size of 100 compared to the right figure with an ensemble size of 800. This indicates that the overlapping phenomenon worsens with more movement, meaning that the structure of tissue and blood flow varying more rapidly can cause more overlapping.

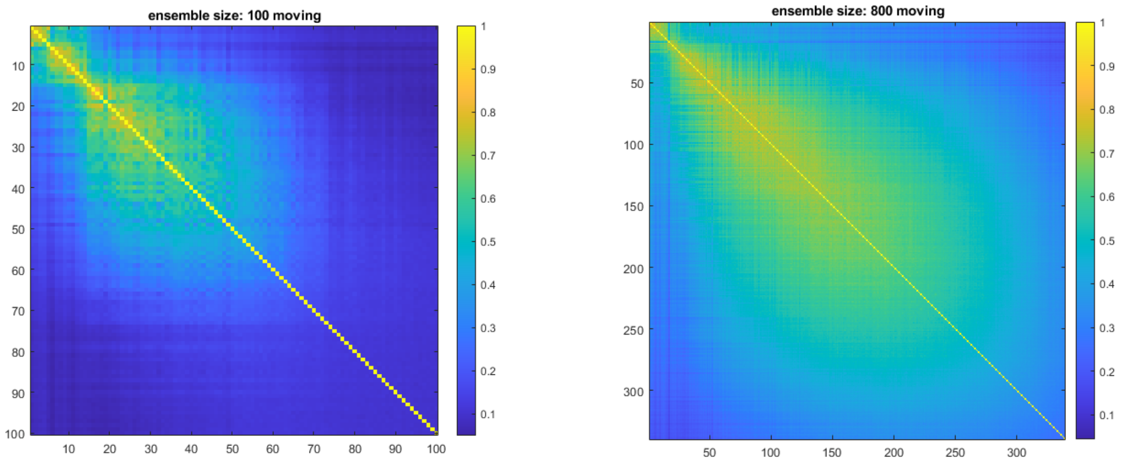

Figure 4.13: Comparison of similarity matrices of U for ensemble sizes of 100 and 800 in a moving dataset (zoomed-in view)

Figure 4.14 compares the similarity matrices of a stationary and a moving dataset with an ensemble size of 800. For the stationary data acquisition, the probe was attached to a rigid arm which was mounted on the operating table so it was very stable. For the moving data acquisition, the probe was moved continuously by hand to scan the brain. Separated subspaces are more pronounced in the left figure for a stationary dataset compared to the right figure for a moving dataset. This is because with spatial information that varies, tissue and blood flow tend to have overlapped spatial characteristics, resulting in overlapped subspaces in the similarity matrix.

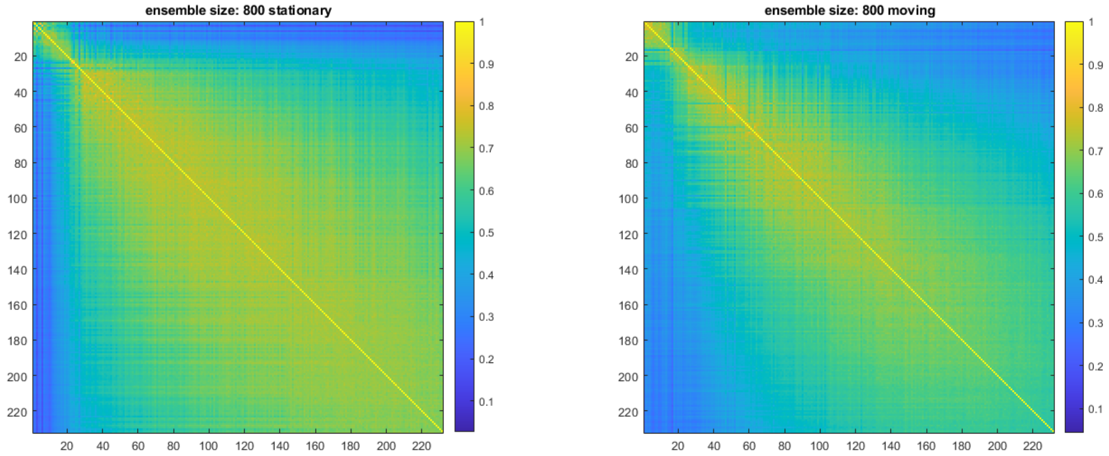

Figure 4.14: Comparison of spatial similarity matrices of U for ensemble sizes of 800 in a stationary dataset and a moving dataset (zoomed-in view). The rest of the view is largely noise.

4.2 Robust PCA clutter filtering

SVD clutter filtering is not always able to completely separate tissue and blood flow components due to their overlapped subspaces on the eigen-domain, as discussed in Chapter 4.1.3. Therefore, Robust PCA clutter filtering, which models the signal matrix as a sum of a low-rank matrix and a sparse matrix, could provide another decomposition perspective to reject tissue clutter.

4.2.1 Choices of λ and μ on threshold selection

As previously discussed in Chapter 3.3 about the theoretical aspects of Robust PCA, there are two things to be optimized: the rank of the L matrix and the sparsity of the S matrix which depend on two parameters λ and μ. λ controls the trade-off between the low rank and sparsity and μ is a constant number which balances the error term. It is important to discover how different combinations of these parameters impact the quality of the resulting images and it could provide guidance for parameter value choices on other datasets.

The metric to evaluate the image quality is the correlation coefficient R. The range of R is between -1 to 1. The closer it gets to 1 or -1, the more similar the two components are. It computes the correlation coefficient between two matrices [43] as Equation 4.2, where in our case A and B are two matrices with a size $n_z \times n_x$. Specifically, A is an SVD clutter-filtered PDI with a rejection threshold of 10% (the first 40 out of 400 singular components are discarded), and B are Robust PCA clutter-filtered PDIs with different λ and μ values. SVD clutter filtering is the most common and widely used method to reject tissue clutter and it has an overall good performance regardless of the overlapped subspaces. The aim of calculating the correlation between the results from these two clutter filtering methods is to test which parameter value combinations can have good performance. The correlation between the Robust PCA-filtered images and the SVD-filtered ones will provide initial guidelines for selecting good parameter values for the Robust PCA algorithm.

$$R = \frac{\sum_m \sum_n \left(A_{mn} - \bar{A}\right)\left(B_{mn} - \bar{B}\right)}{\sqrt{\left(\sum_m \sum_n \left(A_{mn} - \bar{A}\right)^2\right)\left(\sum_m \sum_n \left(B_{mn} - \bar{B}\right)^2\right)}} \tag{4.2}$$

The default parameters are calculated as $\lambda = \frac{0.1}{\sqrt{(max(n_t, n_x \times n_z))}}$, and $\mu = 100 \times \lambda$. As the chosen ensemble length is 400, the lateral dimension n_x is 256, and the depth in the medium in front of the ultrasound probe n_z is 576, thus the default parameters $\lambda = 0.005$ and $\mu = 0.5$. Different values around default parameters are tested and the results are shown in Table 4.2:

The sizes of both L and S are of $(n_t, n_z \times n_x)$, which is 400×147456. Therefore the maximum rank of L is 400, and the maximum cardinality of S is 58982400. Regarding correlation coefficients, it reaches the highest at 0.9355 with $\lambda = 0.002$ and $\mu = 5$ and 30. Since the reference SVD-filtered PDI has a good performance in rejecting tissue clutter, a higher correlation coefficient means that the Robust PCA-filtered PDIs with certain λ and μ values can work better. Overall, the values of λ can more strongly affect the correlation values and the cardinality of S than the value of μ. When λ increases, this trade-off weighting parameter leans towards sparsity, as the cardinality of S becomes less, indicating that S becomes more sparse. The sparsity of S does not necessarily relate to high correlation coefficients. As this table shows, when the cardinality of S becomes very small (less than 1,000,000), the correlation coefficients get negative. When it reaches around half of the full cardinality (29,491,200), the correlation coefficients become higher and closer to 1.

After testing different combinations of λ and μ, $\lambda = 0.002$ and $\mu = 5$ are selected to have the best performance as their correlation coefficient reaches the highest among all combinations that have been tested. The visualization of reconstructed PDIs of L and S is shown in Figure 4.15, with the comparison of the SVD clutter-filtered PDI by a clutter rejection percentage of 10%. With a correlation coefficient similarity of 0.9355, the PDI of S and SVD-filtered PDI look very alike, with most tissue clutter being removed and most blood vessels being kept. On the reconstructed PDI of L, it

μ	λ	Iteration number	Rank(L)	Card(S)	Correlation coeefficients	Computational time
5	0.001	2	400	49104362	0.9287	21.8872
1	0.001	28	29	58561575	0.8585	226.9385
0.5	0.001	42	16	58576931	0.753	333.9717
0.01	0.001	189	11	58391107	0.5936	1568
100	0.002	1	400	26715200	0.9331	11.9973
30	0.002	2	400	26951635	0.9335	23.5944
5	0.002	2	400	28082956	0.9355	23.8451
1	0.002	35	52	58258890	0.9303	305.9845
0.5	0.002	39	45	58334767	0.8836	339.3636
0.01	0.002	57	10	58246308	0.8143	494.0975
5	0.005	2	400	1566166	0.5794	23.6614
1	0.005	10	400	2315343	0.7115	89.7235
0.5	0.005	17	400	2820448	0.7559	105.5275
0.01	0.005	20	400	3034322	0.7497	175.411
5	0.008	2	400	348083	-0.4514	23.5598
1	0.008	7	400	428384	-0.4247	64.5816
0.5	0.008	14	400	516773	-0.4144	125.8938
0.01	0.008	54	400	562552	-0.4323	466.8485
5	0.01	2	400	43071	-0.4744	23.6139
0.01	0.01	53	400	328356	-0.5746	461.0167

Table 4.2: The relations between μ and λ value selections, iteration numbers, rank of L, the cardinality of S, correlation coefficients with SVD-filtered image, and computational time.

can be seen that most tissue is concentrated in the middle upper regions but there are still some vessel-like structures left in the middle of the image.

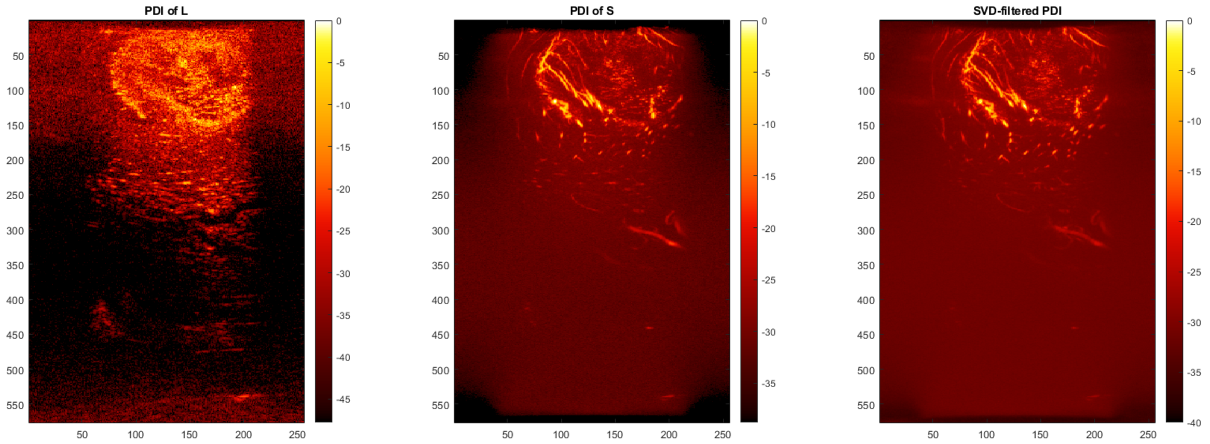

Figure 4.15: PDIs of the reconstructed L matrix, S matrix, and SVD-filtered image with a tissue threshold of 10% for an ensemble size of 400.

There is still some extent of the remaining blood flow signal in L. It would be highly beneficial if the spatial distribution information could be investigated first as we would know if there are correlated spatial subspaces for tissue clutter and potential blood vessels respectively. When comparing their spatial similarity matrices as Figure 4.16 shows, it is obvious that spatial similarity matrices of L and X look very alike. As there are tissue and blood flow spatial subspaces that can be separated from the similarity matrix of X, it is also expected that there is similar information contained in the similarity matrix of L.

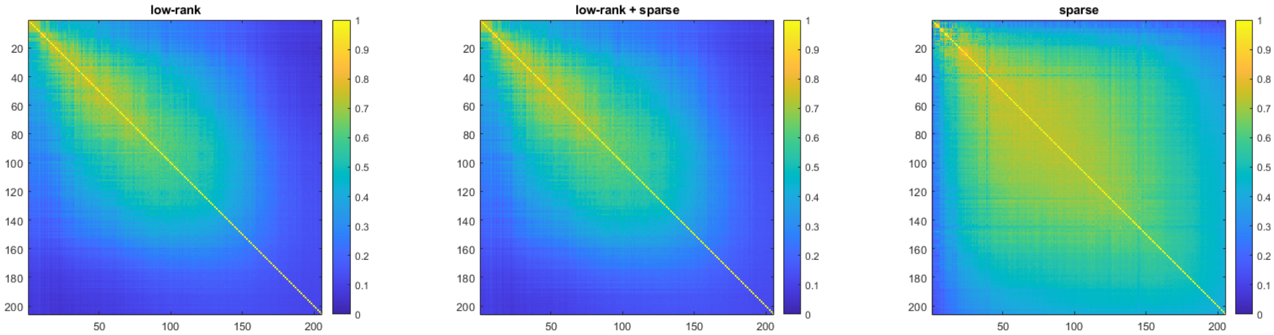

Figure 4.16: Spatial similarity matrices of L, X (X is made up by $L + S$ as discussed in 3.7), and S with a zoomed-in view. The areas out of the zoomed-in view are all blue (similarity value is 0).

As an optimal tissue threshold of 10% is chosen for SVD clutter filtering of X in Figure 4.15, this 10% threshold will also be applied to SVD clutter filtering of L as their spatial similarity maps are indistinguishable. After the filtering, the PDI visualization of refiltered L is shown in Figure 4.17. To enhance the image quality, the refiltered L matrix is added up to S matrix to construct a final image. This image is then correlated with the reference image and it turns out that the correlation coefficient reaches 0.9996, which could indicate that there is more revealed blood flow information. However, a high correlation with the SVD-filtered image is not really the goal. A method that reveals more blood vessels than the SVD may have a lower correlation value. This will be discussed in Chapter 5 Discussion part.

This combination of Robust PCA clutter filtering and SVD clutter filtering could provide insight into extracting blood flow information not only from the sparsity matrix but also from the low-rank matrix to fully extract all the blood flow information.

4.3 ICA clutter filtering

4.3.1 SVD pre-processing

The ICA clutter filtering procedure involves removing the most coherent tissue clutter and non-coherent noise by SVD clutter filtering first, separating the reconstructed Casorati matrix into short time windows, decomposing each window into independent sources, selecting the most relevant ones to blood flow, and summing over the power

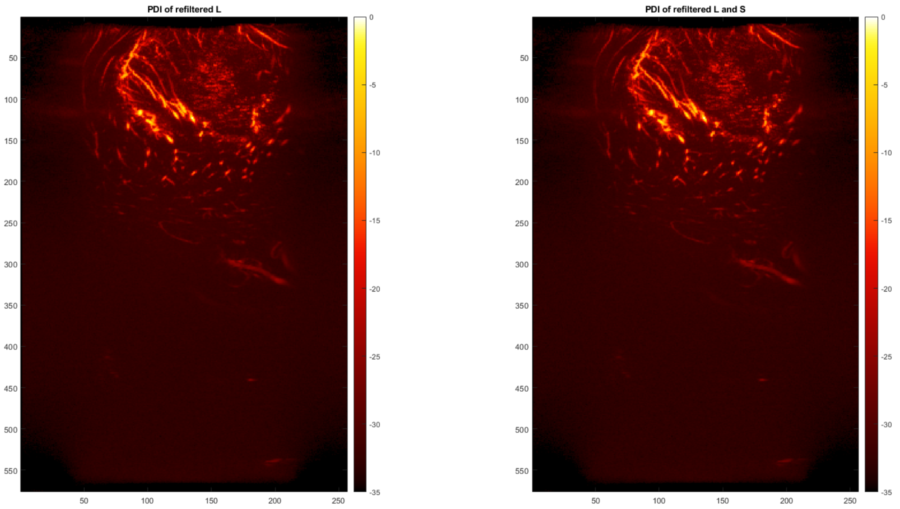

Figure 4.17: Reconstructed PDIs of the refiltered L matrix and the superposition of the refiltered L and S matrix (a stack of frames from 100 to 500).

to reconstruct a PDI. The graphical explanation was previously demonstrated in Figure 3.13.

All the results are tested on an ensemble of 200 frames of a moving dataset. Regarding the prior step of applying SVD clutter filtering to remove the most coherent tissue clutter and non-coherent noise before ICA clutter filtering, two thresholds of 2 and 92 are selected. This means that the first 2 (1%) singular components and the components from 92 to 200 are discarded. This threshold criteria selection is based on the singular value estimator and spatial singular vector estimator as Figure 4.18 shows. 1% threshold is a very low threshold for SVD clutter filtering as usually the threshold is set as around 10%. The reason to select a very low threshold is to remove the most coherent tissue and avoid accidentally removing part of blood flow whose subspaces might overlap in tissue subspaces. The noise threshold is set as $+0.4dB$ higher than the lowest singular component energy ($-36.6236dB$), as the energy level after 92 components is very low. On the spatial similarity map, it can also be observed that the color is very blue on the right side of the second white-dashed line, indicating a low correlation.

4.3.2 Independent component classification

After SVD pre-processing, the reconstructed Casorati matrix of size $n_t \times n_x n_z$ (200×147456) is divided into five short time windows, and the size of each window is 40. The number of independent components is set as 40, and hence the mixing matrix is of 40×40 and the size of independent components is of 40×147456 for each short time window.

It is always hard to sort independent components or select independent components belonging to blood flow based on a quantitative metric. As Chapter 3.4 mentioned, so far there are two methods that have been presented in the literature to sort independent

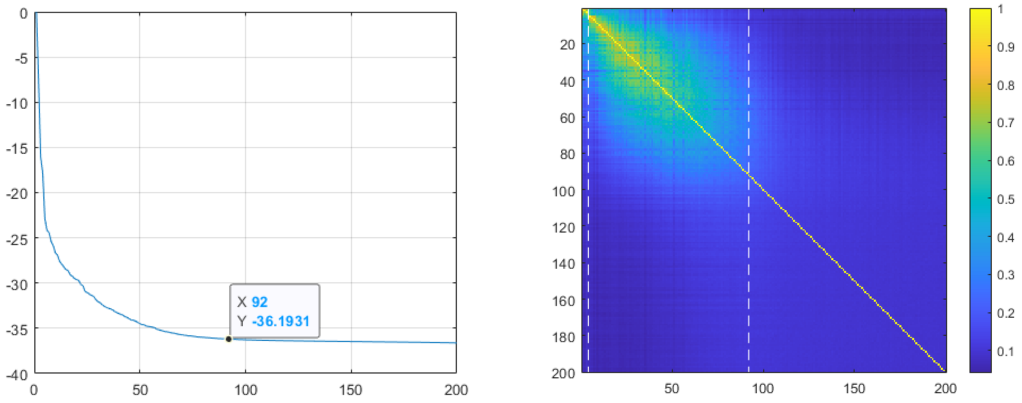

(a) (b)

Figure 4.18: (a) Singular value energy curve in dB. The noise threshold is set as 92 with energy value $-36.1931dB$. (b) Spatial similarity map. Two dashed lines represent thresholds of 2 and 92.

components for ICA clutter filtering on μDopper imaging:

1. Independent components sorting based on correlation coefficients computed between reconstructed power Doppler images created with each individual independent component and a power Doppler image created with all components: the higher the correlation coefficients is, the more likely that the source belongs to tissue clutter [19], and then set a threshold to choose sources belonging to blood flow.

2. Independent components sorting based kurtosis measurement values: the higher the kurtosis value is, the more independent the source is, and the more likely that the source belongs to blood flow as it is assumed that blood flow signals are sparser and thus have higher independency and thus kurtosis than tissue [18]. After sorting, a threshold is set to choose sources belonging to blood flow.

   For this thesis, a new automatic independent components selection method is proposed and has been tested effective on the selected frames:

3. Grouping independent component sources by applying hierarchical agglomerative clustering. This is based on grouping clusters with minimal inner squared distances in a bottom-up approach. The hierarchical agglomerative clustering methodology is explained in Chapter 3.2.5.

This clustering method is applied to 40 independent components in each short time window. The number of clusters is set as 2. It is assumed that one cluster belongs to tissue and another one belongs to blood flow. An example is shown in Figure 4.19. It is observed that among these unsorted independent sources, there are some contain massive tissue clutter and some contain blood flow structures. After clustering independent

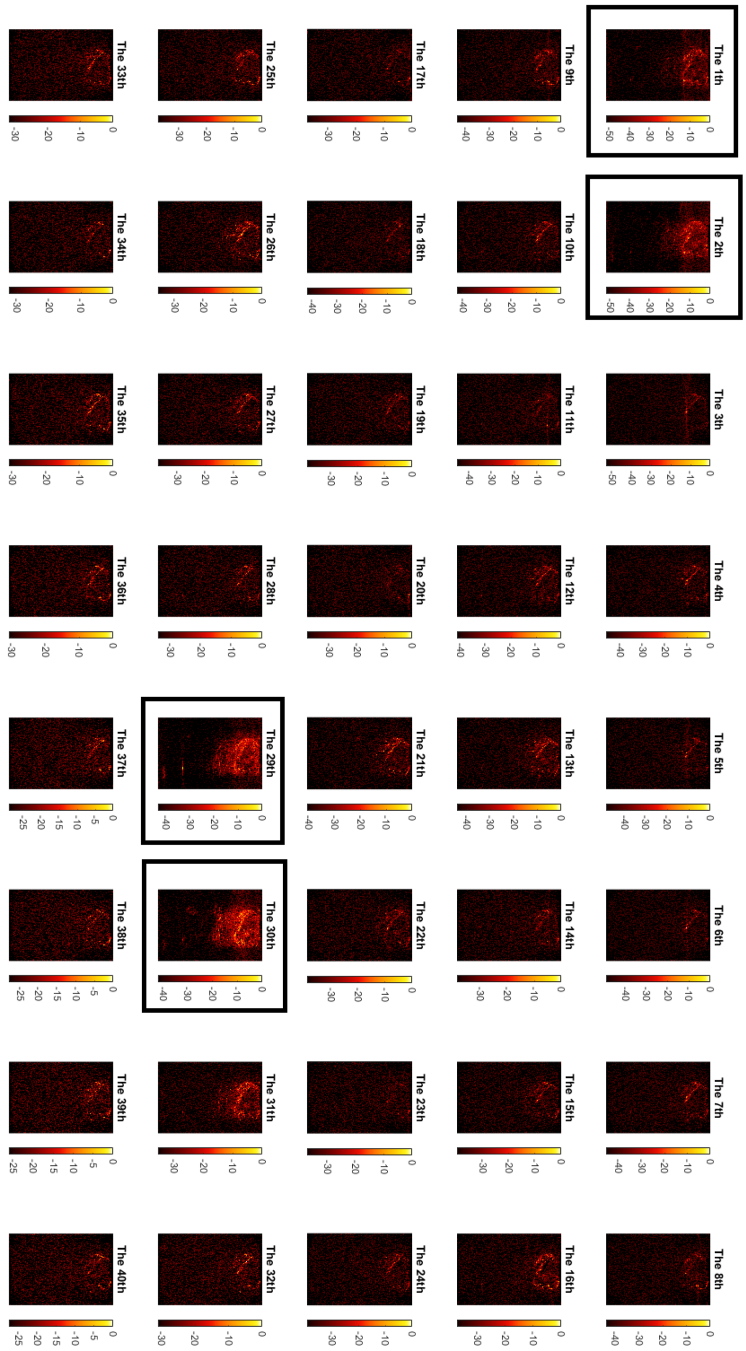

Figure 4.19: Unsorted independent components clustered by hierarchical agglomerative clustering after SVD pre-filtering with an ensemble length of 200. Small windows of size 40 are applied for ICA-clutter filtering and this is the second window.

sources into two groups, the 1^{st}, 2^{nd}, 29^{th}, and 30^{th} sources belong to one group and the rest belong to another group. For the 1^{st}, 2^{nd}, 29^{th}, and 30^{th} sources, tissue clutter are the most outstanding compared to other independent sources. As observed from the

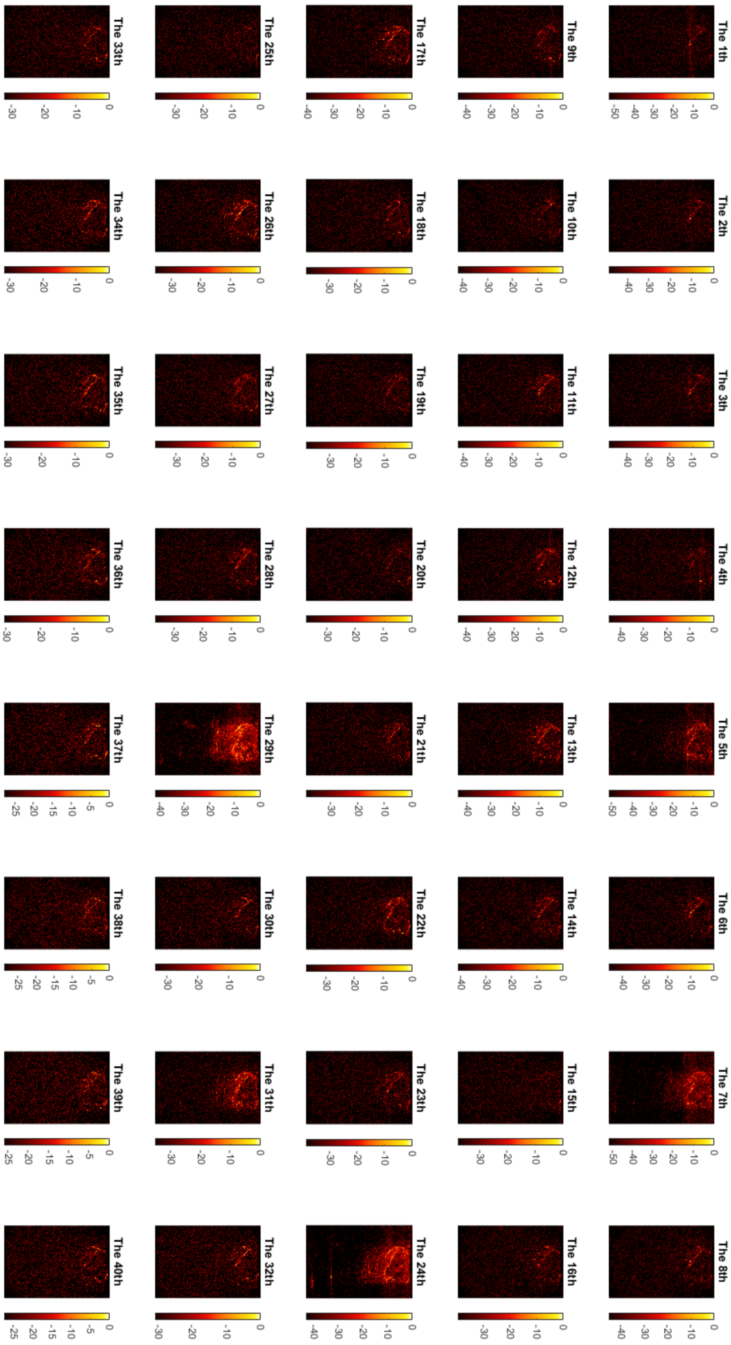

Figure 4.20: Independent components sorted by kurtosis measure, with the first independent component having the highest kurtosis value and the last independent component having the lowest kurtosis value.

figure, most independent sources are related to blood flow. Therefore, when clustering is applied to every window, it is assumed that the cluster with fewer components belongs to tissue and should be removed. The same results also can be discovered in other windows, which shows that this hierarchical agglomerative clustering method can

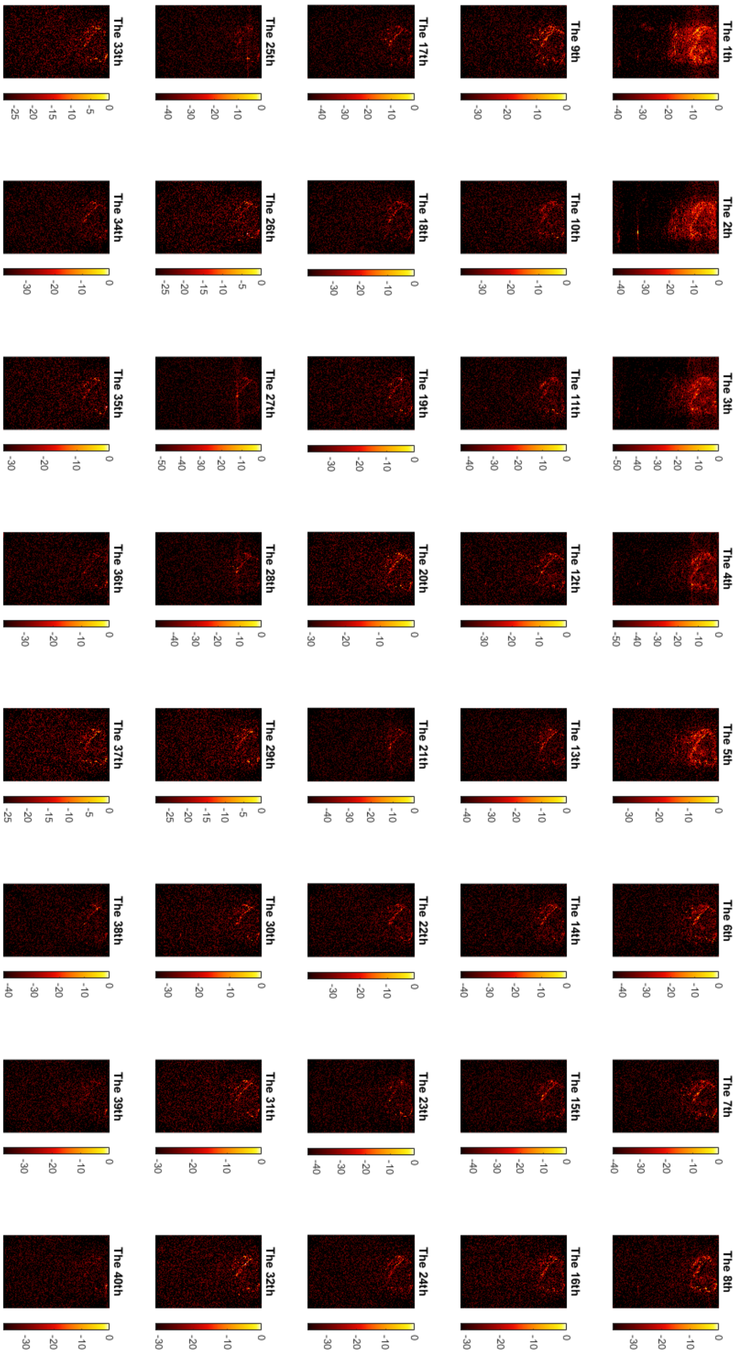

Figure 4.21: Independent components sorted by correlation coefficients, with the first independent component having the highest correlation coefficient and the last independent component having the lowest correlation coefficient.

be effective in grouping sources corresponding to tissue clutter in ICA clutter filtering.

Compared to hierarchical agglomerative clustering, sorting independent sources by kurtosis may not be very effective. In Figure 4.20, the independent sources are sorted by ascending order. It is assumed that higher kurtosis corresponds to blood flow and lower kurtosis corresponds to tissue. However, the result is not ideal as some independent sources with a high kurtosis contain a lot of tissue clutter. For example, for 24^{th} and 29^{th} independent sources, tissue structure can be clearly observed from the middle region, while for $25^{th}, 26^{th}, 27^{th}$, and 28^{th} independent sources with kurtosis values higher than 29^{th} but lower than 24^{th} sources, vasculature can be fairly observed compared to tissue. In an ideal case, the independent source with a bigger index always contains more tissue. This result shows that it is worth discovering other methods of sorting independent sources.

Sorting independent sources by correlation coefficients provides another perspective to sort independent components. Independent components with a low index show a strong correlation with the original μDoppler image. Since the image without clutter filtering is filled with most tissue clutter, high correlation independent sources contain most tissue clutter. By comparing them with their neighbors, it seems that this method can work well. However, a threshold problem of how to separate independent sources also occurs. The number of independent components to be discarded may differ for different windows, and thus it is hard to just have an arbitrary threshold applied to all windows.

Comparing these three methods, hierarchical agglomerative clustering provides a robust and automatic method for selecting independent components corresponding to blood flow without the need for manually choosing parameters to decide them.

4.3.3 Comparisons with SVD clutter filtering

After sorting the independent sources belonging to blood flow and summing them over, a filtered PDI is reconstructed as Figure 4.22c shows. The remaining independent sources consist of most tissue clutter and after summing over the image is shown in Figure 4.22b. SVD pre-filtered PDI as an initial input image is also shown in Figure 4.22 in comparison with them.

To test the performance of ICA clutter filtering, SVD clutter filtering is compared with it. To make fair comparisons, SVD clutter filtering is applied to the same SVD pre-filtered image. The threshold is determined by an automatic estimator based on the spatial similarity matrix of $\mathbf{U}$ as proposed and tested by Baranger *et al.* [14]. For these specific frames, the threshold is set as 22, which means that singular components from 1-22 are considered tissue clutter, and singular components from 23-200 are considered blood flow. The results of collected tissue and blood PDI after SVD clutter filtering are shown in Figure 4.23.

When ICA clutter filtering and SVD clutter filtering are compared in a zoomed-in view as Figure 4.24 shows, it can be observed that their vasculature shows a similar structure, while there is still some tissue clutter concentrated in the middle region within the tumor. The ideal case is that no tissue clutter appears in the middle region. Next, we take a certain row of both images to find out their signal intensity.

After extracting the signal intensity from a certain row which covers not only the blood flow but also the middle-region tissue clutter, the signal is shown in Figure 4.25. From

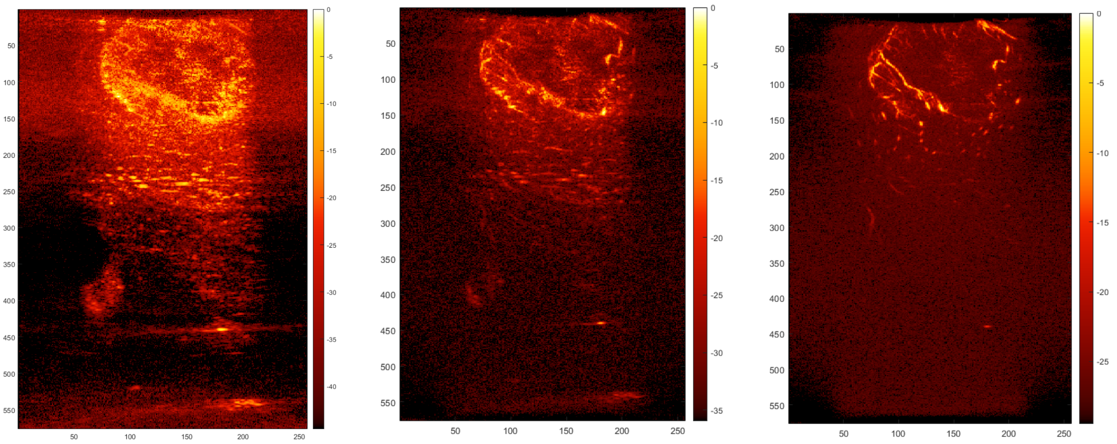

(a) (b) (c)

Figure 4.22: (a): PDI of SVD pre-filtering. The first 2 (1%) and the last 108 components are discarded. (b): Tissue PDI of independent components clustered by hierarchical agglomerative clustering. (c): Blood flow PDI of independent components clustered by hierarchical agglomerative clustering.

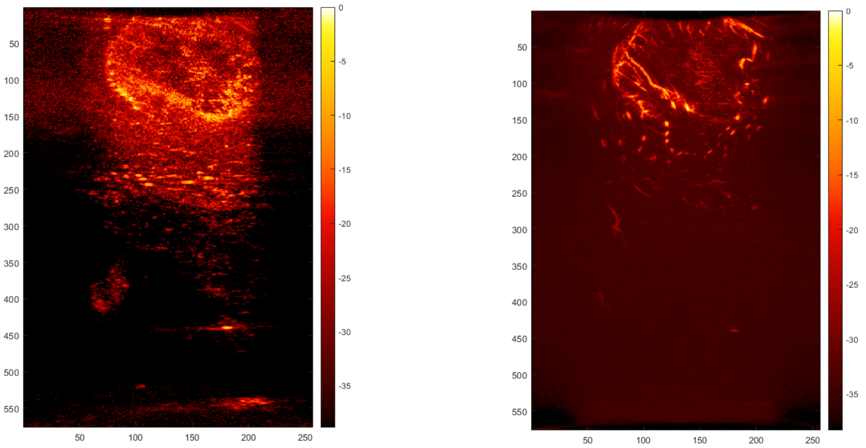

(a) (b)

Figure 4.23: PDI from SVD clutter filtering. The threshold is decided by an automatic spatial estimator and is set as 22. The first 22 singular components are considered as tissue and the last 178 components as blood flow. (a): Tissue clutter PDI. (b): Blood flow PDI.

the x-axis 140 to 170 which corresponds to the tissue clutter, there is a rise for both clutter filtering techniques. The difference between them is that the red dashed line displays a much bigger peak while the blue dashed line shows a much lower peak. For SVD clutter filtering, the tissue clutter signal intensity has almost the same value as other blood flow signals. Compared to ICA clutter filtering, the tissue clutter signal intensity still remains at a relatively low level compared to blood flow signals.

We have explored the middle-region tissue signal intensity, but it is also worth discovering other region parts of the tissue and blood flow. The zoomed-in upper-left view

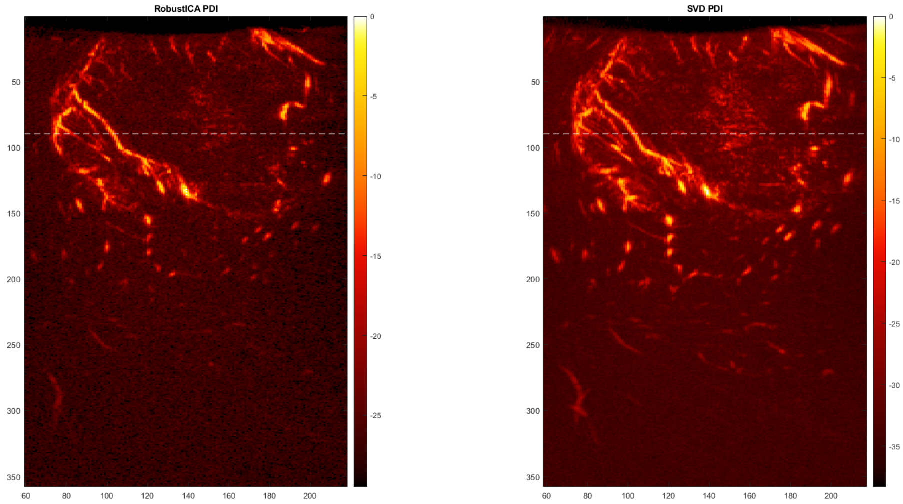

Figure 4.24: Comparison of zoomed-in view with a highlighted line between ICA clutter filtering and SVD clutter filtering.

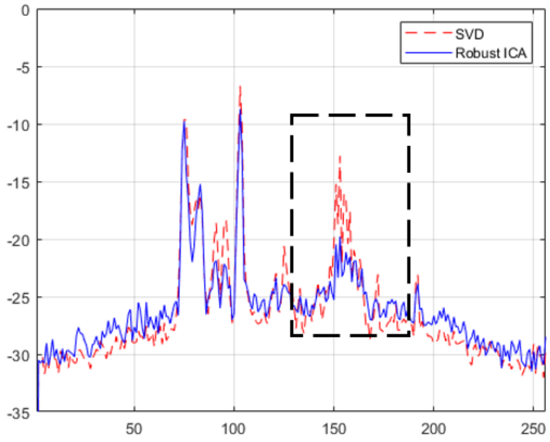

Figure 4.25: Signal intensity of the highlighted line.

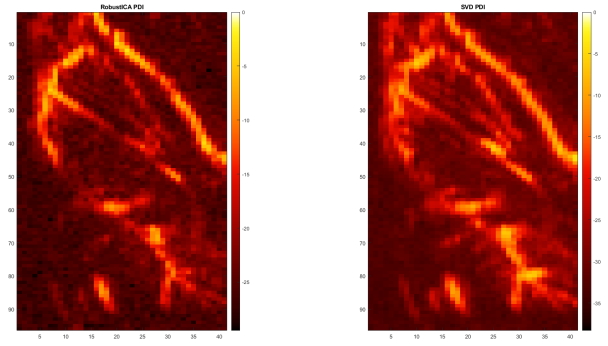

Figure 4.26: Comparison of zoomed-in upper-left view between ICA clutter filtering and SVD clutter filtering.

between ICA clutter filtering and SVD clutter filtering is shown in Figure 4.26. The result of ICA clutter filtering can give a clear blood flow structure, and the result of SVD clutter filtering can reveal more blood vessels. From CNR's perspective, if certain regions of blood flow are selected and their CNRs are calculated, SVD clutter filtering will have a higher value. Because there is no ground truth for blood flow signals, it is hard to distinguish blood flow and tissue clutter in a small region. The blurred area nearby blood flow can be considered as remaining tissue, but it also could be considered as blood flow.

5 Discussion

Freehand movement is challenging for clutter filtering on in-vivo μDoppler ultrasound data, especially when the ground truth is unknown. Challenges and uncertainties include how to decide thresholds to distinguish tissue and blood flow, how to decide ensemble lengths for different clutter filtering techniques, how to tune parameters for Robust PCA clutter filtering, how to decide the number of independent components, how to sort independent sources corresponding to blood flow signals, and how to make fair comparisons for the images filtered by different techniques. This chapter discusses answers to the research questions posed at the start of this thesis and potential improvements for future work.

Clutter filtering techniques on freehand μDoppler in-vivo ultrasound data: The goal of this thesis is to explore and compare three clutter filtering techniques (SVD, Robust PCA, and ICA clutter filtering) on freehand μDoppler in-vivo ultrasound data. For SVD clutter filtering, there are several estimators being explored, including arbitrary thresholding, singular value estimators based on singular energy, spatial singular vector estimators based on spatial similarity matrices or clustering on spatial singular vectors, and temporal singular vector estimators based on the frequency spectra. All estimators can perform on a global perspective or block-wise perspective, depending on the datasets and the purpose of use. The thresholds also differ for different datasets, different ensemble sizes, and different estimators. Deciding the threshold based on the spatial similarity matrix could be the most promising method as the threshold can be determined by finding the optimal fitting for the juxtaposed matrices and the spatial similarity matrix in an automated way.

Through the research on theories and testing on μDoppler data, Robust PCA clutter filtering is applied by proper parameter choices of λ and μ. Furthermore, the image is enhanced by combining SVD and Robust PCA clutter filtering for not only extracting the sparsity matrix but also extracting the remaining blood flow information from the low-rank matrix. The image evaluation is done by correlating an SVD clutter filtered image to Robust PCA clutter filtering. There could be better ways to test image qualities with different parameter values as an SVD clutter filtered image is not ideal and some better performed images might have a lower correlation. For ICA clutter filtering, it is applied by selecting appropriate independent sources by using hierarchical agglomerative clustering. In this thesis, an ensemble size of 200 and window size 40 is used for ICA clutter filtering. This is based on a paper from Wahyulaksana *et al.* [18]. For our data, these sizes work well for our moving dataset to produce images with good performance. When the ensemble size is increased to 400 and the window size keeps to 40, the performance is decreased as there is more blood flow information being wrongly removed. After SVD pre-processing, the reconstructed Casorati matrix is divided into 10 windows with a size of 40 for each window. One of the reasons for the poorer performance could be the number of clusters. The default number of clusters is set as two, with one corresponding to tissue and another one to blood flow. This number could be very small that some tissue and blood flow independent components with very close spatial features could be treated as the same cluster.

Regarding computational complexity, Robust PCA clutter filtering with $\lambda = 0.002$ and $\mu = 5$ for an ensemble size of 400 takes around 23 seconds and has very similar computational time for SVD clutter filtering with the same ensemble size. For ICA clutter filtering combined with clustering for an ensemble size of 200 and clustering window of 40, the computational time takes around 160 seconds. This is much longer than other clutter filtering techniques. Overall, for a general application, SVD clutter filtering is more suitable as there will only be one threshold to decide. Robust PCA clutter filtering needs to have two parameters to decide and ICA clutter filtering needs sorting or clustering on independent components. If only a specific stack of frames is needed to apply clutter filtering, then Robust PCA and ICA could provide more perspectives in decomposing signal matrices as they do not take the arbitrary assumption that tissue and blood flow have orthogonal subspaces.

Overlapped subspaces on the eigen-domain: One of the sub-questions is: "How to illustrate that tissue and blood flow have overlapped subspaces on the eigen-domain". Overlapping causes difficulty in finding an optimal threshold to separate tissue and blood flow. It is shown by the power spectrum density of temporal singular vectors, where tissue and blood flow are observed to have overlapped frequency spectra under a certain frequency amplitude. If the threshold is set at a certain frequency, it could be the case that some blood flow can be discarded and some tissue clutters can be kept. Another demonstration is based on spatial similarity matrices where in most fast-movement cases subsquares are not distinguishable and cannot be easily separated.

Freehand motion effect: For this sub-question: "How does freehand motion affect the threshold selection criteria", thresholds to separate tissue and blood flow are compared between stationary datasets and moving datasets. Stationary datasets tend to have more stable thresholds than moving datasets for different stacks of frames. The effect of probe movement can be seen in the correlation matrix of the Casorati matrix, which shows the correlation between each frame and its neighboring frames. The correlation matrix of a moving dataset concentrates high correlation values around the diagonal while correlation has overall very high values for a stationary dataset. Because of the probe movement, spatial distributions vary over time, and this can cause a phenomenon that subspace squares on spatial similarity maps have more distinct characteristics for stationary datasets than for moving datasets. Therefore, we need an automated method as each threshold cannot be manually selected because of high time costs. In this thesis, freehand motion can cause subspaces to overlap spatialtemporally for SVD clutter filtering. The proposed ICA clutter filtering with clustering on blood flow can work adaptive to reject tissue clutter and keep blood flow in an automated manner and the image quality shows comparably good performance. The image provides a clear vasculature with a great amount of blood flow. Robust PCA clutter filtering investigation only focuses on parameter tuning for a specific stack of frames, and it aims to provide an automated way to decide parameter values in the future.

Fair comparisons: The last research question is about evaluating image quality and making fair comparisons among different clutter filtering techniques. In general, making fair comparisons is difficult, as the extracted signal intensity and range could be varying for different techniques. When constructing power Doppler images, the power intensity of each pixel is divided by the maximum power intensity among all pixels. Therefore, the range of power intensity for every pixel is always within a certain value from $0dB$ to around $-80dB$. When we visualize PDIs, if all images are set for the same dynamic ranges ($0dB$ to $-40dB$), the images are like Figure 5.1a. If the averaged intensity from some part of the background is set as the limit of dynamic ranges, the images look as Figure 5.1b shows. The comparisons are fairer when the background color is set at the same level. Regarding the metrics SNR and CNR to evaluate the image quality, we need to have a critical judgment on whether those values best describe the image quality especially when ground truth is unknown. If some tissue clutter appears very nearby the blood flow area, their CNR value will be considered as blood flow CNR, which might lead to a misunderstanding conclusion for comparisons. When using SNR, we need to make sure that their noise and aimed signals are on the same intensity level, or the SNR evaluation would be not effective. Signal amplitude levels can be moved upwards or downwards to be aligned to avoid this problem. Besides that, the image quality can differ from different applications. In this thesis, SNR and CNR are not used for evaluating image quality as the comparison conclusion can be directly derived from extracted signal intensity. For example, in Figure 4.25, signals corresponding to tissue located inside the tumor are easily compared between two clutter filtering techniques as the amplitude makes a big difference.

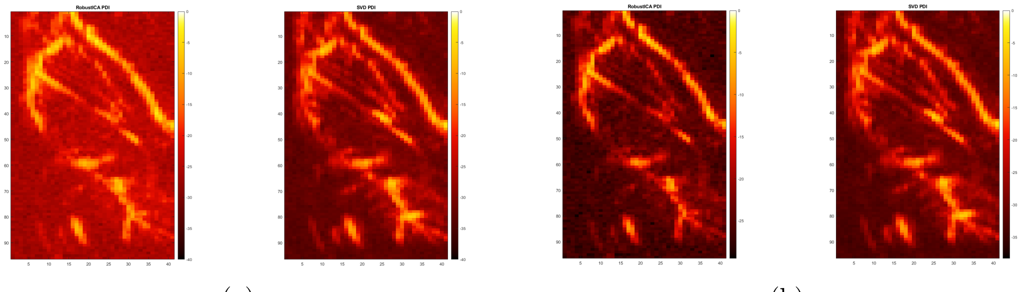

(a) (b)

Figure 5.1: An example of two pairs of PDI comparisons. (a): fixed dynamic range from $0dB$ to $-40dB$. (b): adjusted dynamic range from $0dB$ to $-29dB$ and $0dB$ to $-38dB$.

Future work: There are some possible improvements for the work in this thesis. A block-wise filtering approach could be further explored on different datasets for SVD clutter filtering. The correlation matrix of the Casorati matrix and spatial similarity matrix of fast movement and slow movement in the same image region could be tested and compared to further understand how motion affects threshold selection criteria. In terms of Robust PCA clutter filtering, the method used to evaluate image quality for different parameter settings involves correlating the filtered image with an SVD-filtered image as a reference. The results are promising, as the quality of the reference image shows good performance. A high correlation between Robust PCA-filtered images and the reference image indicates high image quality. However, since the reference image filtered by SVD is not ideal, this comparison method still needs improvement. It aims to find another method to evaluate Robust PCA image quality and compare the best-filtered image with images filtered by other clutter filtering techniques. For ICA clutter filtering, currently the number of clusters is set as two, including the tissue cluster and blood flow cluster. Future work could involve testing on more clusters and selecting correlated clusters corresponding to blood flow. Another possible improvement could be the metric to evaluate the image quality. More metrics could be tested on μDoppler data, for example, generalized-CNR (gCNR), etc.

6

Conclusion

μDoppler ultrasound imaging is an HFR ultrasound imaging modality that is suitable to provide high spatiotemporal resolution ultrasound vasculature images. Clutter filtering is an essential step in μDoppler data processing to reject tissue clutter signals and keep blood flow information as much as possible. Freehand movement of the probe make clutter filtering on in-vivo datasets challenging to acquire high-quality filtered images as the spatial content changes over the temporal dimension when the probe moves continuously by hand. This thesis has explored three clutter filtering techniques: SVD, Robust PCA, and ICA clutter filtering. The summarized methods for these techniques are presented in Table 6.1.

Besides exploring these techniques and methods, SVD clutter filtering is also used to investigate how freehand motion affects threshold selection and demonstrate the overlapped subspaces on the eigen-domain. The result shows that freehand motion can cause unstable threshold criteria for different stacks of frames and the subspaces for tissue and blood flow overlap spatiotemporally. Robust PCA clutter filtering combined with SVD clutter filtering provides new insight into extracting blood flow information not only from the sparse matrix but also from the low-rank matrix. ICA clutter filtering, with hierarchical agglomerative clustering assisted, could reconstruct a good quality PDI with great amounts of blood flow and less tissue clutter compared to SVD clutter filtering. It can be used as an automated way for clutter filtering. Overall, for a general application, SVD clutter filtering is more suitable as there will only be one threshold to decide. Robust PCA clutter filtering needs to have two parameters to decide and ICA clutter filtering needs sorting or clustering on independent components. If only

Clutter filtering techniques		
Name	**Estimator**	**Description**
SVD	Arbitrary thresholding	Based on singular value energy (dB)
	Spatial singular vector	Based on the correlation matrix of U; based on clustering on U
	Temporal singular vector	Based on the PSD of V
Robust PCA	Entire ensemble size	The signal matrix is modeled as a sum of a low-rank component, a sparse component and the additive noise
	Small window	
	SVD+RobustPCA on entire ensemble size	
	SVD+RobustPCA on small window	
ICA	Entire ensemble size	ICA seeks to transform the data onto a basis with statistically independent vectors
	Small window	
	SVD+RobustICA on entire ensemble size	
	SVD+RobustICA on small window	

Table 6.1: Overview of clutter filtering techniques

a specific stack of frames is needed to apply clutter filtering, then Robust PCA and ICA could provide more perspectives in decomposing signal matrices as they do not take the arbitrary assumption that tissue and blood flow have orthogonal subspaces. Future work could involve improving the blood flow extraction accuracy for ICA clutter filtering combined with clustering, working on better ways to evaluate Robust PCA filtered images with different parameter values, and fair comparison metrics.

Bibliography

[1] F. M. Benslimane, M. Alser, Z. Z. Zakaria, A. Sharma, H. A. Abdelrahman, and H. C. Yalcin, "Adaptation of a mice doppler echocardiography platform to measure cardiac flow velocities for embryonic chicken and adult zebrafish," *Frontiers in bioengineering and biotechnology*, vol. 7, p. 96, 2019.

[2] S. T. Torp-Pedersen and L. Terslev, "Settings and artefacts relevant in colour/power doppler ultrasound in rheumatology," *Annals of the rheumatic diseases*, vol. 67, no. 2, pp. 143–149, 2008.

[3] P. Kruizinga, P. van der Meulen, A. Fedjajevs, F. Mastik, G. Springeling, N. de Jong, J. G. Bosch, and G. Leus, "Compressive 3d ultrasound imaging using a single sensor," *Science advances*, vol. 3, no. 12, p. e1701423, 2017.

[4] L. Verhoef, S. Soloukey, F. Mastik, B. S. Generowicz, A. J. Vincent, E. M. Bos, J. W. Schouten, C. M. Dirven, C. I. De Zeeuw, S. K. Koekkoek *et al.*, "Reconstructing human cerebral vasculature in 3d with high frame rate, freehand 2d doppler ultrasound using optical tracking," in *2022 IEEE International Ultrasonics Symposium (IUS)*. IEEE, 2022, pp. 1–4.

[5] "basic ultrasound, echocardiography and doppler ultrasound." [Online]. Available: https://folk.ntnu.no/stoylen/strainrate/Basic_Doppler_ultrasound

[6] J. Sevec, "What is hierarchical clustering?" 2023, accessed on June 7^{th}, 2023. [Online]. Available: https://www.mtab.com/blog/what-is-hierarchical-clustering

[7] P. Song, A. Manduca, J. D. Trzasko, and S. Chen, "Ultrasound small vessel imaging with block-wise adaptive local clutter filtering," *IEEE transactions on medical imaging*, vol. 36, no. 1, pp. 251–262, 2016.

[8] C. Chilowsky and P. Langevin, "Procédés et appareils pour la production de signaux sous-marins dirigés et pour la localisation à distance d'obstacles sous-marins," *French patent*, vol. 502913, 1916.

[9] M. Tanter and M. Fink, "Ultrafast imaging in biomedical ultrasound," *IEEE Transactions on Ultrasonics, Ferroelectrics, and Frequency Control*, vol. 61, pp. 102–119, 2014.

[10] S. Soloukey, A. J. Vincent, D. D. Satoer, F. Mastik, M. Smits, C. M. Dirven, C. Strydis, J. G. Bosch, A. F. van der Steen, C. I. D. Zeeuw, S. K. Koekkoek, and P. Kruizinga, "Functional ultrasound (fus) during awake brain surgery: The clinical potential of intra-operative functional and vascular brain mapping," *Frontiers in Neuroscience*, vol. 13, 1 2020.

[11] S. Soloukey, L. Verhoef, P. J. van Doormaal, B. S. Generowicz, C. M. Dirven, C. I. De Zeeuw, S. K. Koekkoek, P. Kruizinga, A. J. Vincent, and J. W. Schouten,

"High-resolution micro-doppler imaging during neurosurgical resection of an arteriovenous malformation: illustrative case," *Journal of Neurosurgery: Case Lessons*, vol. 4, no. 19, 2022.

[12] M. Halliwell, "Doppler ultrasound: Physics, instrumentation and signal processing," 2000.

[13] J. Bercoff, G. Montaldo, T. Loupas, D. Savery, F. Mézière, M. Fink, and M. Tanter, "Ultrafast compound doppler imaging: Providing full blood flow characterization," *IEEE transactions on ultrasonics, ferroelectrics, and frequency control*, vol. 58, no. 1, pp. 134–147, 2011.

[14] C. Demené, T. Deffieux, M. Pernot, B. F. Osmanski, V. Biran, J. L. Gennisson, L. A. Sieu, A. Bergel, S. Franqui, J. M. Correas, I. Cohen, O. Baud, and M. Tanter, "Spatiotemporal clutter filtering of ultrafast ultrasound data highly increases doppler and fultrasound sensitivity," *IEEE Transactions on Medical Imaging*, vol. 34, pp. 2271–2285, 11 2015.

[15] Q. Huang, Y. Luo, and Q. Zhang, "Breast ultrasound image segmentation: a survey," *International journal of computer assisted radiology and surgery*, vol. 12, pp. 493–507, 2017.

[16] Q. Huang, F. Yang, L. Liu, and X. Li, "Automatic segmentation of breast lesions for interaction in ultrasonic computer-aided diagnosis," *Information Sciences*, vol. 314, pp. 293–310, 2015.

[17] K. Xu, X. Guo, Y. Sui, V. Hingot, O. Couture, D. Ta, and W. Wang, "Robust pca-based clutter filtering method for super-resolution ultrasound localization microscopy," in *2021 IEEE International Ultrasonics Symposium (IUS)*. IEEE, 2021, pp. 1–4.

[18] G. Wahyulaksana, L. Wei, J. Schoormans, J. Voorneveld, A. F. Van der Steen, N. De Jong, and H. J. Vos, "Independent component analysis filter for small vessel contrast imaging during fast tissue motion," *IEEE Transactions on Ultrasonics, Ferroelectrics, and Frequency Control*, vol. 69, no. 7, pp. 2282–2292, 2022.

[19] J. Tierney, J. Baker, D. Brown, D. Wilkes, and B. Byram, "Independent component-based spatiotemporal clutter filtering for slow flow ultrasound," *IEEE transactions on medical imaging*, vol. 39, no. 5, pp. 1472–1482, 2019.

[20] B. S. Generowicz, "Improving ultrafast doppler imaging using subspace tracking," 2019. [Online]. Available: http://ens.ewi.tudelft.nl/

[21] R. Wildeboer, F. Sammali, R. Van Sloun, Y. Huang, P. Chen, M. Bruce, C. Rabotti, S. Shulepov, G. Salomon, B. C. Schoot *et al.*, "Blind source separation for clutter and noise suppression in ultrasound imaging: Review for different applications," *IEEE Transactions on Ultrasonics, Ferroelectrics, and Frequency Control*, vol. 67, no. 8, pp. 1497–1512, 2020.

[22] D. C. Fisher and S. A. Altobelli, "Physical principles of doppler ultrasound: Measuring movement with sound," *Postgraduate Medicine*, vol. 78, no. 6, pp. 118–130, 1985.

[23] J. M. Rubin, "Power doppler," 1999.

[24] E. Mace, G. Montaldo, B. F. Osmanski, I. Cohen, M. Fink, and M. Tanter, "Functional ultrasound imaging of the brain: Theory and basic principles," *IEEE Transactions on Ultrasonics, Ferroelectrics, and Frequency Control*, vol. 60, pp. 492–506, 2013.

[25] D. Babcock, H. Patriquin, M. LaFortune, and M. Dauzat, "Power doppler sonography: basic principles and clinical applications in children," *Pediatric radiology*, vol. 26, no. 2, pp. 109–115, 1996.

[26] L. Demi, "Practical guide to ultrasound beam forming: Beam pattern and image reconstruction analysis," 9 2018.

[27] M. Ashikuzzaman, C. Belasso, M. G. Kibria, A. Bergdahl, C. J. Gauthier, and H. Rivaz, "Low rank and sparse decomposition of ultrasound color flow images for suppressing clutter in real-time," *IEEE transactions on medical imaging*, vol. 39, no. 4, pp. 1073–1084, 2019.

[28] Q. Huang and Z. Zeng, "A review on real-time 3d ultrasound imaging technology," *BioMed research international*, vol. 2017, 2017.

[29] M. H. Mozaffari and W.-S. Lee, "Freehand 3-d ultrasound imaging: a systematic review," *Ultrasound in medicine & biology*, vol. 43, no. 10, pp. 2099–2124, 2017.

[30] J. Baranger, B. Arnal, F. Perren, O. Baud, M. Tanter, and C. Demene, "Adaptive spatiotemporal svd clutter filtering for ultrafast doppler imaging using similarity of spatial singular vectors," *IEEE Transactions on Medical Imaging*, vol. 37, pp. 1574–1586, 7 2018.

[31] N. Zhang, M. Ashikuzzaman, and H. Rivaz, "Clutter suppression in ultrasound: performance evaluation and review of low-rank and sparse matrix decomposition methods," *Biomedical engineering online*, vol. 19, no. 1, pp. 1–38, 2020.

[32] M. Kim, Y. Zhu, J. Hedhli, L. W. Dobrucki, and M. F. Insana, "Multidimensional clutter filter optimization for ultrasonic perfusion imaging," *IEEE transactions on ultrasonics, ferroelectrics, and frequency control*, vol. 65, no. 11, pp. 2020–2029, 2018.

[33] E. J. Candès, X. Li, Y. Ma, and J. Wright, "Robust principal component analysis?" *Journal of the ACM (JACM)*, vol. 58, no. 3, pp. 1–37, 2011.

[34] M. Grant, S. Boyd, and Y. Ye, "Cvx: Matlab software for disciplined convex programming (web page and software)," 2009.

[35] J.-F. Cai, E. J. Candès, and Z. Shen, “A singular value thresholding algorithm for matrix completion,” *SIAM Journal on optimization*, vol. 20, no. 4, pp. 1956–1982, 2010.

[36] Y. E. Nesterov, “A method of solving a convex programming problem with convergence rate o\bigl(k^2\bigr),” in *Doklady Akademii Nauk*, vol. 269, no. 3. Russian Academy of Sciences, 1983, pp. 543–547.

[37] S. Boyd, N. Parikh, E. Chu, B. Peleato, J. Eckstein *et al.*, “Distributed optimization and statistical learning via the alternating direction method of multipliers,” *Foundations and Trends® in Machine learning*, vol. 3, no. 1, pp. 1–122, 2011.

[38] F. Yao, J. Coquery, and K.-A. Lê Cao, “Independent principal component analysis for biologically meaningful dimension reduction of large biological data sets,” *BMC bioinformatics*, vol. 13, pp. 1–15, 2012.

[39] A. Hyvärinen and E. Oja, “Independent component analysis: algorithms and applications,” *Neural networks*, vol. 13, no. 4-5, pp. 411–430, 2000.

[40] P. Comon, “Independent component analysis, a new concept?” *Signal processing*, vol. 36, no. 3, pp. 287–314, 1994.

[41] V. Zarzoso and P. Comon, “Robust independent component analysis by iterative maximization of the kurtosis contrast with algebraic optimal step size,” *IEEE Transactions on neural networks*, vol. 21, no. 2, pp. 248–261, 2009.

[42] P. C. V. Zarzoso. Robustica algorithm for independent component analysis. [Online]. Available: https://www.i3s.unice.fr/~zarzoso/robustica.html

[43] T. M. Inc., “corr2 2-d correlation coefficient, image processing toolbox,” Natick, Massachusetts, United States, 2022. [Online]. Available: https://nl.mathworks.com/help/images/ref/corr2.html

Appendix A

A.1 Image visualization from singular components

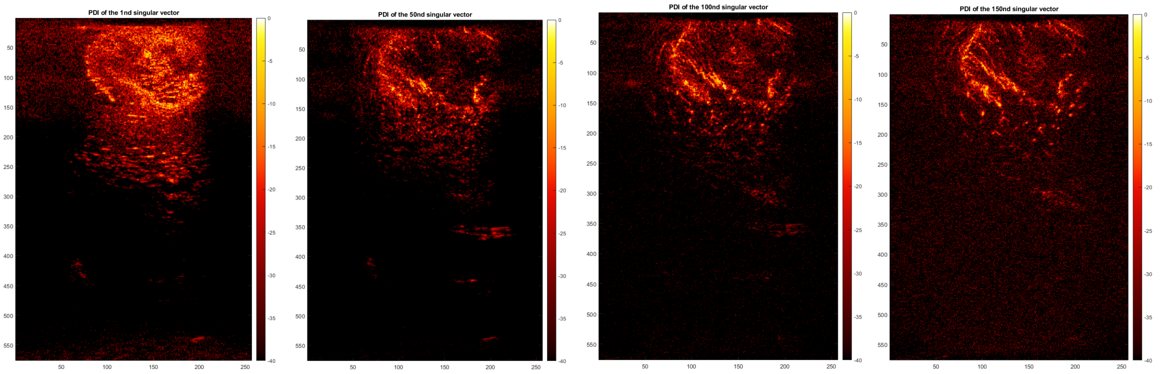

(a) 1^{st} singular component visualization.

(b) 50^{th} singular component visualization.

(c) 100^{th} singular component visualization.

(d) 150^{th} singular component visualization.

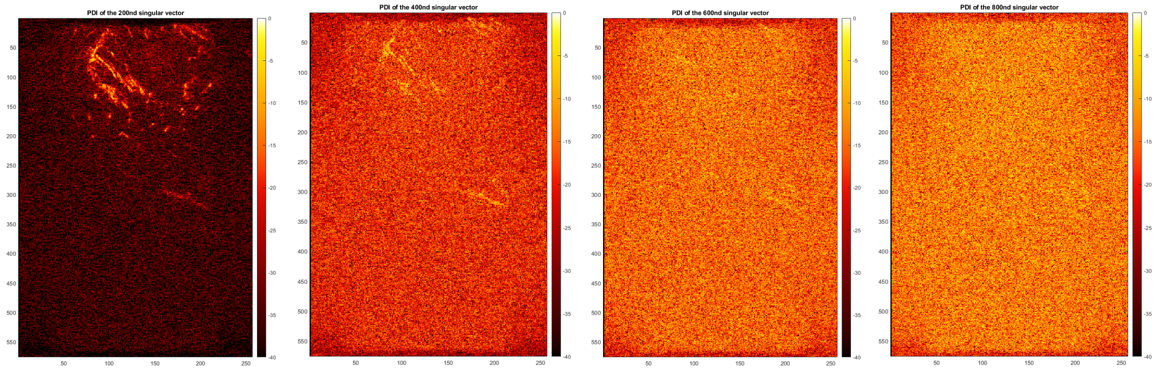

(e) 200^{th} singular component visualization.

(f) 400^{th} singular component visualization.

(g) 600^{th} singular component visualization.

(h) 800^{th} singular component visualization.

Figure A.1: Image visualization of singular components for a moving dataset with an ensemble length of 800. The 1^{st} singular component visualization contains most tissue clutter. From 1^{st} to 150^{th}, there is more pronounced blood flow. After 200^{th}, more noise appears.